Joint Centre for Mesoscale Meteorology, Reading, UK

Stacked slantwise convective circulations

K. A. Browning
D. Chapman
R. S. Dixon

Internal Report No. 129
NWP Scientific Paper No. 62

April 2001

Met Office Joint Centre for Mesoscale Meteorology Department of Meteorology
University of Reading PO Box 243 Reading RG6 6BB United Kingdom
Tel: +44 (0)118 931 8425 Fax: +44 (0)118 931 8791
www.metoffice.com

Designed and produced by the Met Office © Crown copyright 2001 01/0240 The Met Office logo is a registered trademark.

Revised, April 2001

Stacked slantwise convective circulations

By K.A. Browning*, D Chapman and R.S. Dixon
University of Reading

Summary

It is well known that classical (ana) cold fronts tend to be characterised by mesoscale circulations in which upright line convection feeds a layer of concentrated rearward slantwise ascent. Occasionally, however, as in the case study presented in this paper, two and sometimes more of these mesoscale circulations coexist within the same cold-frontal zone. The two slantwise circulations described here were observed to be stacked one above the other with a vertical wavelength less than 2km. Although it is often suspected that the circulations at ana-cold fronts are enhanced by mesoscale processes such as conditional symmetric instability (CSI) or ΔM-adjustment, it is notoriously difficult to discriminate between these circulations and the larger-scale transverse circulation within which they are embedded.. The occurrence in this study of multiple circulations with small vertical scale helps to distinguishe them from the large-scale circulation and this has motivated our detailed examination of this case.

Mesoscale circulations of the kind described here are difficult to detect: numerical weather prediction (NWP) models, even high-resolution models, do not usually represent them, and conventional observations do not show them clearly. This study takes advantage of observations from a very-high-resolution microwave Doppler radar plus a high-resolution analysis of UHF wind profiler radar data, analysed in the context of output from an operational mesoscale

*Corresponding author: Joint Centre for Mesoscale Meteorology, Department of Meteorology, University of Reading, PO Box 243, Reading, Berkshire, RG6 6BB, UK.

NWP model. The study defines the mesoscale structure of the event sufficiently carefully to provide a basis for future idealized modelling studies to investigate the possible roles of CSI and ΔM-adjustment, both of which appear to play some part in the maintenance of the circulations.

1. Introduction

(a) *The theoretical background*

In a baroclinic atmosphere, moist convection may take a variety of forms depending on the relative gravitational and inertial stability to vertical and horizontal motions. Pure gravitational instability may be released by upright motions and pure inertial instability by horizontal motions. Conditional symmetric instability (CSI) arises from the combination of gravitational and inertial accelerations in a baroclinic atmosphere and this may be released by slantwise motions (Bennetts and Hoskins 1979). Such motions are referred to as slantwise convection.

As described in the recent review of CSI by Schultz and Schumacher (1999), slantwise and upright convection may coexist in regions that are unstable to both. The slantwise convection extends over a horizontal scale of about 100 km, which is more than an order of magnitude greater than that for upright convection. It yields vertical velocities of tens of cms^{-1}, more than an order of magnitude smaller than the updraughts within upright convection. If an initially gravitationally and inertially stable baroclinic atmosphere is destabilised, then symmetric instability will appear prior to pure gravitational instability (Emanuel, 1994). However, the larger growth rate of gravitational instability implies that if both instabilities are present then the release of pure gravitational instability (leading to upright convection) will tend to dominate in time. Alternatively, these instabilities may interact such that the release of one type of instability preconditions the atmosphere for the other type of instability. The warm sectors

of baroclinic cyclones are often potentially unstable to either or both slantwise and upright convection, as noted by Emanuel (1994).

Two mechanisms for the interaction of symmetric and pure gravitational instability in frontal rainband development are discussed by Xu (1986). He considers the process of frontal-rainband development suggested by Bennetts and Hoskins (1979) as 'downscale' development of CSI. In this scenario, the release of CSI causes the middle troposphere to become unstable to upright gravitational instability. In the alternative, 'upscale' development, small-scale upright convection occurs first; this stabilises the atmosphere to upright gravitational instability and meso-β-scale slantwise convection then occurs. Even in an atmosphere stable to CSI it is still possible for upright convection to trigger slantwise convection, but through an inertially stable process known as ΔM adjustment. In this process upright convection lifts low-level air upwards, leading to subgeostrophic momentum anomalies in the middle troposphere which are removed by slantwise convection (Holt and Thorpe, 1991; Fischer and Lalaurette 1995).

It is widely recognised that the representation of moist convection within numerical models represents one of the great challenges standing in the way of the improvement of weather and climate prediction. The scales of convective motions sit uneasily between being partially resolved and being sub-grid scale processes whose effects need to be parametrized: there is a danger of double counting. The nature of the modelling challenge is changing, and at the same time the opportunity to address it is improving, as a result of the development of high-resolution mesoscale numerical weather prediction (NWP) models in which the individual convective motions are being increasingly but still not yet entirely resolved. The current mesoscale version of the Met Office's operational forecast model (Unified Model) already has a horizontal grid length as small as 12km and work is underway in the Joint Centre for Mesoscale Meteorology (JCMM) aimed at reducing the resolution of a new version of the model to about 2km (P.Clark

and H Lean, personal communication). An important ingredient for progress in this area is the development of a better understanding of the nature of both upright and slantwise circulations and the ways in which they interact. These issues are being addressed within the JCMM as part of a balanced programme of theoretical, observational and modelling studies (Gray et al 2000). The present paper represents an observational contribution to this programme, drawing especially upon the high-resolution 10cm wavelength Doppler radar at the Rutherford-Appleton field site at Chilbolton in southern England (Goddard et al 1994).

b) Introduction to the case study

In this paper we present a case study of an ana-cold front which travelled eastwards across the Doppler radar at Chilbolton, and other radars in southern England, displaying several well-defined layers of slantwise convection associated with lines of very shallow upright convection. The fact that upright and slantwise convection can co-exist in cold-season ana-cold fronts was recognized by Browning and Harrold (1970) and Browning and Pardoe (1973). That this often occurrs in the UK is now widely accepted by the forecasting community (Met Office 1997,Ch.7). The conceptual model in Fig.1 shows how the shallow upright line convection at the surface cold front feeds a layer of rearward-directed slantwise ascent. Browning (1990) suggests that the line convection shown in Fig.1 is due to the SCF propagating into an almost neutrally – rather than unstably-stratified air mass, thereby generating upright convection that is forced rather than free. The forced nature of the convection is considered to account for the often rather 2-dimensional nature of the line convection. We shall adopt a different perspective in the present study by recognising that the boundary-layer air mass ahead of the SCF, while close to neutral stratification, does have a small and possibly significant degree of potential instability. We shall also be taking note of the existence of potential instability behind the main SCF.

Figure 2 gives a previously published example of a scan from the Doppler radar at Chilbolton through an intense circulation of this kind (Browning et al 1997), showing a rearward system-relative flow (red and yellow) of warm air within the pre-frontal boundary layer rising as line convection at the surface cold front (range 25 km) and then ascending slantwise behind the front (as part of the red and yellow flow toward the left of the diagram). The continuous lines in Fig.2 are streamlines, calculated assuming approximately 2-dimensional flow and horizontal flow at both the ground and a height of 6km. The fact that the momentum anomalies do not line up perfectly with the streamlines above 3km and beyond 60 km suggests the existence of errors in the streamlines that may be attributable to limitations in the 2-dimensional assumption; however, the overall flow pattern is believed to be qualitatively correct. The slantwise ascent of prefrontal warm air to the left of the line convection is also seen to be augmented by the ascent of some of the cold air which previously had been catching up with the cold front at low levels (the blue flow between 1 and 2km). Shallow but very intense radar echo was associated with the line convection and this case was embedded within much weaker echo due to the mainly stratiform ascent elsewhere. Recent studies have indicated the likely role of CSI and ΔM-adjustment in generating or augmenting the slantwise ascent in this and in other similar situations (Dixon 2000). Evidence has been presented by Dixon which suggests that the inability of the model, even with a 12 km horizontal grid, to resolve these processes properly, can delay the development of the transverse circulation. Poor vertical resolution of the model in the middle troposphere may be the main deficiency because, according to Persson and Warner (1993), a minimum resolution of 170m is necessary to resolve CSI driven circulations.

The striking feature of the new case selected for study here is not only the coexistence of linked upright and slantwise convective circulations as in Fig.2, but also the coexistence of two or more sets of such circulations, with the slantwise flows associated with one of the ciruclations situated beneath the slantwise flows of the other circulation. This leads to what we refer to as vertically

stacked slantwise circulations as distinct from the single major circulation portrayed in Fig.2. One of the difficulties in interpreting observed circulations is in distinguishing slantwise motions that are due to CSI or ΔM-adjustment from the rather larger-scale ageostrophic circulations that occur in association with frontogenesis. Schultz and Schumacher (1999) argue that it is impossible to distinguish them. Certainly the distinction is blurred when the circulation is as deep as that in Fig.2. However, in the present study the ascending limbs of the individual stacked slantwise circulations are separated by as little as 2km in the vertical and are thus more likely to be attributable to a mesoscale process such as CSI or ΔM-adjustment. Normally it would be difficult to obtain definitive radar observations of such shallow circulations except at very close range. In this study, however, it has been made possible by the fact that the Chilbolton radar uses a 25-metre dish which provides a one-third degree beam width and thus a resolution of 300m at 60 km range (Goddard et al 1994). The resolution in the radial direction is 75m, although only every fourth range gate has been used, giving an effective radial resolution of 300m.

The case study is presented in four sections. First, in Section 2, there is a brief overview of the synoptic context based on some routinely available observational data and output from the mesoscale version of the operational Met Office Unified Model. This 12-km-grid model failed to resolve either the upright convection or the multiple fine-scale slantwise circulations but it represented the slightly larger-scale context well. The detailed mesoscale observations from the Doppler radar at Chilbolton are then presented in Section 3 and interpreted to reveal the structure and inter-relationship of the multiple upright and slantwise convective circulations. This is followed by an observational synthesis in Section 4 and a general discussion and theoretical interpretation in Section 5.

2. The case study: context provided by operationally available data

Before presenting the very detailed observations of the slantwise circulations from the Chilbolton radar (Section 3), we first make use of operationally available synoptic and sub-synoptic data so as to provide the overall context. The main sources of data are very-short-range forecasts from the mesoscale version of the Unified Model, imagery from the geostationary satellite Meteosat, surface rainfall patterns from part of the UK weather radar network and time-height wind plots from the UHF wind-profiler radar at Met Office, Camborne.

The subject of the case study is the vigorous cold front that travelled eastwards across the British Isles on 10 February 2000. Figure 3 shows model-derived plan views of the frontal system at 0900 UTC as the surface cold front (SCF) was crossing central England. Figure 3(a) shows a plot of surface pressure and fronts; Fig.3(b) shows the associated bands of cloud as seen in the infra-red imagery. Figure 3(c) shows that ahead of the SCF there was a belt of air with high wet-bulb potential temperature (θ_w) in the boundary layer corresponding to a warm conveyor belt (WCB). The SCF itself was sharply defined, with a large change in θ_w and temperature (not shown) across it. Over southern England there was also a significant along-front gradient of θ_w (i.e. along the axis of the WCB) corresponding to a warm-frontal zone.

Of the two major belts of high cloud shown in Fig. 3(b), one was along the leading edge of the WCB and the other – the subject of this study – was along part of the trailing edge of the WCB in association with an ana-cold frontal circulation. The deepest part of this cold-frontal cloud area is marked by a dashed envelope in Fig. 3(a) and comparison with Fig.3(c) shows that this cloud feature is closely associated with (and behind) the region of most concentrated θ_w gradient. The model cross-sections shown later in Fig.4 are along the line through the Chilbolton radar and almost perpendicular to the cold front, as shown

in Fig.3(a). These sections are across the sharp cold front and through the middle of the dashed cold-frontal cloud feature.

The region of ascent responsible for the dashed cold-frontal cloud feature was ahead of an eastward-moving upper-level potential-vorticity (PV) anomaly/streamer that extended southwards to the west of the British Isles. An analysis of quasi-geostrophic vertical motion at 700 mb (not shown) demonstrated that there was significant forcing of vertical motion from upper-tropospheric levels, presumably related to this PV streamer. Figure 3(d) shows that, in part of the streamer over western Ireland, the surface where PV = 2 PV units, corresponding to the tropopause, reached down to 6km. A cross-section presented shortly shows that fragments of PV>2 PV units extended down to 4km within a tropopause fold which tended to undercut the cold-frontal cloud band.

The set of model-derived cross-sections in Fig.4 are for the time corresponding to Fig.3. Figure 4(a) shows air with a θ_w of greater than 8°C (stippled) reaching down to the surface over a 100 km-wide strip (the WCB), followed by a sharp SCF, and a shallow layer of potential instability where the westerly component of wind shear caused a tongue of low-θ_w air at 1.5 km to overrun higher - θ_w air nearer the surface. We show later that there was shallow line convection here. Figure 4(b) shows the tropopause depression at the northwestern (left-hand) edge of the section, with the PV-2 air down to 6km and blobs of PV-2 extending within a tropopause fold down to 4km as mentioned before. Values of PV in excess of 1 PV unit associated with this fold are shaded in Fig.4(b). At lower levels there are also a few areas with PV > 1 PV unit due to diabatic effects. Some of these were associated with part of the cold-frontal ascent shown schematically by the ascending arrow. The arrow is shown first rising near-vertically at the SCF and then at a shallow angle between a height of 1½ and 3km. This is the region where the Chilbolton radar revealed the slantwise circulations (Section 3). Figure 4(b) shows that this region of diabatic PV is

separated from the high PV along the axis of the tropopause fold by a strip of slightly negative PV, the axis of which is drawn dashed.

Figure 4(c) shows the parallel-front flow increasing with height in the warm air above the cold-frontal zone, with a southwesterly upper-level jet (J) of almost 60 m s^{-1} at 8km. There is strong cyclonic shear across the frontal zone, especially near the surface. Ahead of the SCF, Fig.4(c) shows a low-level jet (LLJ) with southwesterly winds reaching 30 m s^{-1}, whilst behind the SCF there is a minimum in this component (labelled N).

The model-derived transverse-front component of the wind is shown in Fig.4(d). The frontal system was travelling at 16 m s^{-1} and so the shaded areas in Fig.4(d) correspond to rearward relative flow, consistent with the inferred region of ascent highlighted by the right-hand arrow (same arrow as in other frames in Fig.4). The other arrow in Fig.4(d) highlights a locally enhanced region of forward relative flow extending from the region of the tropopause fold. Figure 4(e) shows that the air associated with this fold was very dry; however, the leading part of this region of forward flow, as highlighted by the arrow, becomes increasingly moist perhaps because of the evaporation of precipitation falling from the overlying region of ana-cold frontal ascent. Various features identified in Figs.4(a-e) are superimposed in Fig.4(f) to clarify their relationships.

The surface rainfall distributions associated with the frontal system at 06, 08 and 10 UTC are shown in Figs.5(a-c). The general area of rain is quite broad, although it narrows with time. Embedded within it there are patches of heavy rain including some that are elongated in the front-parallel direction . An unknown proportion of the bands of apparently heavy rain (eg the red bands in southwest England towards the rear of the rain areas in Figs.5(b) and 5(c)) are artefacts caused by the detection of a strong bright-band anomaly, but other bands correspond to a narrow cold-frontal rainband due to line convection at the SCF.

There have been many observational studies of such narrow rainbands and a recent study by Wakimoto and Bosart (2000) contains an up-to-date list of references.

Successive hourly positions of the dominant narrow cold-frontal rainband, derived from a series of 15-minute images like those in Figs. 5(a-c), are plotted in Fig.5(d). As we show later, there were actually two bands of line convection, L1 and L2, one more intense than the other. In the northern half of Fig.5 the dominant line is L2 whereas in the southern half the dominant line is L1 (the echo line that apparently extends L2 into the southern area in Fig.5(c) is due mainly to the bright-band artefact). The detailed analysis shown later concentrates on the features in the southern half of Fig.5 where the stronger line convection, L1, is seen to be broken up into major line segments. Segments of line convection can be traced back to the earliest times in Fig.5 in areas to the west of southwest England where the background rainfall was initially weak and patchy. Evidence for the existence of some line convection, L2, behind L1 in the southern part of Fig.5 is presented later, but L2 was too weak or too shallow in this region to produce trackable narrow cold-frontal rainband segments on the weather radar network display.

According to Fig.5(d) the line convection, L1, passed over the UHF radar at Camborne at around 0630 UTC. Time-height records of the front-parallel and front-perpendicular components of the wind during and after the passage of the line convection over Camborne are given in Figs. 6(a) and (b). These plots have enhanced time resolution (5-min data smoothed over 15 min) compared with that of the standard operational output (values every 30 min). They show wind patterns that are broadly similar to the corresponding portions of the model-derived spatial cross-sections in Figs.4(c) and (d). Model-derived time-height sections over Camborne itself, plotted in Figs.6(c) and (d), enable a more precise comparison to be made. (The model plots have been derived from hourly samples and at 25 mb intervals, which is substantially less than the model

resolution in the bottom 2km, but using full-resolution data would probably not change the picture very much). The comparison confirms that the model was doing moderately well in resolving the broad velocity structure, albeit with a delay of about 1 hour, but that it failed to resolve significant details of the transverse circulation. Particularly interesting aspects of these transverse circulations revealed by the UHF radar but not by the model are the *not just one, but two* rearward-sloping layers of system-relative rearward flow (layers of enhanced ana-cold frontal ascent S1 and S2) highlighted in Fig. 6(b) by the solid and dashed white arrows, respectively. Just beneath each of these flows there are corresponding layers of strong winds corresponding to forward flow relative to the 16 m s^{-1} system velocity (see the solid and dashed black arrows in Fig.6(b)). The ascending part of the first of the two circulations, S1, (the solid white arrow) is believed to have been fed by the line convection, L1, that crossed Camborne at around 0630 UTC. The low-level convergence (confluence)associated with L1 shows up well in Fig.6(b). The ascending part of the second slantwise circulation, S2, (dashed white arrow) followed 2½ hours (140 km) after the first but there is no clear evidence of well organised low-level confluence that might have been associated with any line convection, L2. A few hours later these same circulations crossed over Chilbolton at which time S2 was, as we show in Sec. 3, intermittently triggering a definite region of line convection, L2, a mere 20 km behind L1.

3. Case study: mesoscale observations from the Chilbolton radar

(a) Vertical radar cross-sections

The clearest evidence of the stacked slantwise circulations is provided by vertical, so called range-height-indicator (RHI), scans by the Chilbolton radar obtained perpendicular to the cold frontal zone. These were part of complete sets of RHI scans obtained at nominally 18° intervals around 360° which were interspersed with so-called plan-position-indicator (PPI) scans made every 28

minutes. A sequence of the front-perpendicular RHI scans showing Doppler velocity, obtained between 0822 and 1111 UTC, is shown in Fig 7. Some of the scans are towards azimuth 309° and others are 180° apart, ie towards 129° (strictly speaking the 129° scan was reconstituted from a pair of closely-spaced scans on either side of this direction). All the scans in Fig.7 have been reproduced so that northwest (the rear of the frontal zone) is to the left and southeast is to the right. The earliest RHI is at the foot of the diagram and the subsequent RHIs plotted above it are displaced to the left by a distance approximately proportional to the 16 m s^{-1} velocity of the frontal system so as to keep the line convection, L1, at the same location (see vertical dotted line running through the entire figure). The RHIs obtained at 1005, 1033 and 1112 UTC correspond to those scanned toward the southeast and this is why they are displaced relative to the other RHIs.

The light blue areas in Fig.7 are where the strength of the winds is similar to the system velocity and, assuming a 2-dimensional steady-state structure, would be where the air is neither descending nor ascending rapidly. The warmer colours (green, yellow, orange, red) correspond to system-relative flows from right to left whilst the dark blue areas correspond to flows from left to right. Since these colours occur in layers most of which slope upwards from right to left, they imply rearward-sloping ascent in the warm-coloured layers and forward-sloping descent in the dark blue layers. There are two main layers of slantwise ascent, with corresponding layers of insignificant ascent or weak slantwise descent beneath each of them. (There is a third layer above S1, seen most clearly in the 1033 UTC scan, which we shall not consider in detail). The axis of the higher of the two main layers of slantwise ascent, referred to as S1, is highlighted by a solid line and the lower layer of slantwise ascent (S2) by a dashed line. Each layer of slantwise ascent is less than 1km deep and the axes of S1 and S2 are separated in the vertical by between 1.3 and 2.5 km. This compares well with the vertical separation of 2.0km when S1 and S2 passed over the Camborne

UHF radar (Fig.6b). A similar separation was also evident from a UHF radar at Dunkerswell (not shown) about midway between Camborne and Chilbolton.

The layer of slantwise ascent, S1, was connected more or less clearly to the region of upright line convection, L1, which lofts boundary-layer air up into the layer of slantwise ascent. The clearest evidence of the upright convection L1, feeding the slantwise ascent, S1, can be seen in the scans at 0851, 0919 and 1005 UTC. Assuming the flow to be approximately 2-dimensional within the plane of these sections, the gradient in the line-of-sight velocity near L1 (vertical dotted line) is such as to imply convergence below ½ km and divergence between 1½ and 2¼ km. The implied low-level convergence is quite strong, corresponding to a change in transverse velocity of about 10 m s^{-1} over 1km (blue to red) at 0919 UTC. The associated updraughts in L1 are highlighted in Fig.7 by the almost vertical lines connected to the layer of slantwise ascent, S1. Similar vertical lines have been drawn on scans at other times where the evidence is less persuasive because of missing low-level data at long range (at 0822 and 1033 UTC), or because of an unscanned region close to the radar (at 0948 UTC). Unequivocal evidence for upright convection, L2, feeding slantwise ascent, S2, is generally missing in the RHI scans except possibly at 0919 UTC at 50 km range where there is divergence between ½ and 1½ km and convergence below ½ km. However, the convergence here is very weak, corresponding to a velocity change of only a few m s^{-1} (light blue to dark blue). Better Doppler evidence of the reality of these line-convection features is shown later in the PPI scans in Fig.8. Reflectivity data also presented in this later figure show precipitation cores associated with the line convection and although the segmentation of these cores shows that there are clearly local departures from 2-dimensionality, the inference of a line of convection line-elements is supported.

Vigorous line convection such as that shown in the introduction (Fig.2), can be identified in terms of reflectivity in RHI scans from the typically 2km-high columns of high reflectivity, sometimes exceeding 50 dBz (not shown). Similarly

strong signatures in the RHI scans were missing on the present occasion. The only RHI for which there was a clear reflectivity signature of strong upright convection was that at 0919 UTC when a column of 40 dBz echo (maximum ~ 45dBz) in association with L1 extended up to 1 km at a range of 27 km (not shown) corresponding to the marked convergence/divergence pattern seen in Fig. 7. Convective echoes associated with L1 were even weaker at 0822 (20 dBz echo at 80 km range), 0851 (30 dBz at 52 km), and 1005 UTC (34 dBz at 15 km towards 129°). The reflectivity-based evidence for significant upright convection was weaker still for L2 and even at 0948 UTC, when there was some evidence of upright convection from the convergence/divergence pattern (Fig.7), there was only a rather broken-up column of 30 dBz reflectivity. As we show later in Fig. 8(d), there were gaps between the updraught cells comprising the line convection and so it was possible for the RHI scans to miss the main cores, but the fact remains that the echo cores were very weak.

b) Plan radar sections

Plan displays of Doppler (ie radial) velocity for two times are shown in Figs.8(a) and (c). The scans were made at 1-deg elevation so that the beam rose above 1km beyond 60 km range. Reflectivity plots at the corresponding times for the boxed sub-areas are shown in Figs.8(b) and (d). The reflectivity plots mainly exclude regions contaminated by bright-band effects. These scans each took 6 minutes to obtain, starting at north and then rotating anticlockwise. As a result some features to the north of the radar are seen twice, almost 6 minutes apart, (eg one of the red echoes in Fig.8(d)).

The Doppler display obtained between 0827 and 0833 UTC (Fig.8(a)) shows a relatively simple velocity pattern associated with a largely homogeneous region of winds veering with height in the low-level jet (LLJ) ahead of the SCF associated with L1. Peak velocity in the LLJ is 35 m s^{-1} from 230° at a height of 800m (corresponding to a range of about 50km). The first sign of the approach

of L1 within range of the Chilbolton radar is the linear zone of Doppler velocity decreasing with range (identified by the dotted line in Fig.8(a)) associated with the thin line of 30 dBz raincells shown in Fig.8(b). The decrease in velocity was associated with the region of divergence centred at 1½ km in the upper part of the line convection, a signature which became better defined as the line came closer to the radar.

By the time of the scan made between 0924 and 0930 UTC in Fig.8(c,d), L1 can be seen to have advanced to within 30 km of the radar and L2 can be seen about 20km or more behind L1. Their positions are highlighted in Fig.8(c) by dotted lines from which it is clear that L1 is broken into two major segments separated by a large step. The larger of the two L1 segments was associated with a well-defined line of convective cells producing small cores of heavy precipitation, as shown in Fig.8(d) by the red areas with reflectivity close to 40 dBz. The L1 segment, to the southwest of the radar (not shown in Fig.8(d)), produced weaker reflectivity cores (35 dBz) but the earlier history of this segment does show up with good continuity in Fig.5(d). Part of a line of weak precipitation cores associated with L2 is also seen towards the top left quadrant of Fig.8(d), 15 to 20km behind L1. The high reflectivity in the top left corner itself is due to the bright band.

The Doppler velocity pattern in Fig.8(c), although showing clear discontinuities along the axes of L1 and L2, is not straightforward and it requires detailed explanation. Along L2 the change in velocity across the line is consistent with across-line divergence: this is because the scan at this range was at a height of about 1 km and was intersecting the upper part of the line convection (which as shown by the 0919 UTC RHI in Fig.7(a) was very shallow). The same may apply to the smaller of the two L1 segments in Fig. 8(c), although here the viewing angle was such that the decrease in Doppler velocity across the line is strongly affected by the veer and shear in the wind across the line. The pattern of Doppler velocity along the larger of the two L1 segments in Fig. 8(c), is rather

different from that along the other L1 segment in that the change in Doppler velocity is consistent with convergence along part of its length. This is mainly because the 1° elevation scan at this range was below ½ km and intersected the lower part of the line convection. As seen in the RHI at 0919 UTC in Fig.7, the low-level convergence at L1 does indeed extend from the surface up to about ½ km.

Viewed on a broader scale, the aspect of Fig.8(c) that distinguishes it most clearly from Fig.8(a) is the way in which the red area of strongly approaching Doppler velocities evolves from a single maximum associated with the prefrontal LLJ in Fig.8(a) to a multiplicity of red maxima in Fig.8(c); the most easterly of these maxima, just ahead of L1, is still due to the southwesterly prefrontal LLJ, but the small maximum seen 40 km west of the radar is due to strong low-level westerlies coming in just behind L1.

The PPI scans in Fig.8 (a-d) have been used mainly to identify the lines of upright convection, L1 and L2. The PPI scan in Fig.8(e) is introduced to draw attention instead to the layers of slantwise convection, S1 and S2, associated with L1 and L2, respectively. This PPI was obtained by scanning at the higher elevation angle of 1.5° (compared with 1.0° for Figs.8(a-d)) within the southeastern sector as the upright line convection and associated layers of slantwise convection travelled away from the radar. The beam overshot both lines of upright convection at this time. Moreover, because the component of the slope of the layers was in the opposite sense to the inclination of the beam, this meant that the scan was able to intersect both layers, S1 and S2. The dotted lines in Fig.8(e) show the axes of the layers of minimum velocity away from the radar corresponding to S1 and S2. Subtraction of the 16 m s^{-1} (line-normal) system velocity shows that these were in fact layers of maximum rearward system-relative flow (rearward sloping ascent) which were embedded within a region of nearly stationary or weakly forward system-relative flow. The shape of the dotted lines in Fig.8(e) is consistent with layers of slantwise circulation that

slope upwards not only from southeast to northwest but to some extent also from northeast to southwest. The dotted lines show that the wind anomalies extend across the entire domain (diameter of radar coverage is 190km) thereby indicating the large lateral extent of both slantwise circulations.

An attempt has been made to infer a vertical profile of the winds in Fig.8(e) by combining measurements made due south and east of the radar after compensating for the slope of the layers (1 in 70 along 300°). Because of the assumptions that had to be made in this analysis, the resulting wind hodograph in Fig.8(f) is only approximate; nevertheless it gives a useful indication of the rearward flow (ie towards the northwest) within layers S1 and S2, relative to the 16 m s^{-1} propagation velocity of the layers themselves as shown by the blue arrow. These circulations in the transverse-front direction are seen to be embedded within a thermal wind shear, with winds increasing strongly with height in the parallel-front direction.

4. Synthesis and discussion of the observed structure and evolution of the line convection and slantwise convection.

The following paragraphs synthesize the findings from the previous sections:

(i) At many intense cold fronts such as the one shown in Fig. 2 , the scale of the transverse circulation makes it impossible to distinguish the contribution that slantwise convection makes from that due to frontogenesis. Slantwise convection is, however, believed to lead to circulations with smaller height scales. This was the reason for examining the present 10 February case in which multiple (usually 2; occasionally more) slantwise circulations, with slopes of typically 1 in 70, were observed stacked one above the other, with a

small vertical spacing of about 2km more plausibly attributable to slantwise convection.

(ii) One of the slantwise circulations, designated S1, tended to dominate for much of the time as it crossed southern England: this was so from the time it passed over the UHF radar at Camborne (see Figure.6(b)) to the time it was observed by the Chilbolton radar (Fig.7). The maximum velocity differential between the rearward and the underlying forward flow components of the circulation was typically 10 m s^{-1}. The rearward ascending component, S1, was fed by line convection which, although not as vigorous as the 3km-deep line convection in Fig.2, nevertheless was detected most of the time by the Chilbolton radar rising as nearly upright convection to about 2km (Fig.7). The large lateral extent of the line convection was confirmed by the radar network which showed stepped line segments extending all the way from the English Channel to Yorkshire. These stepped line segments are also seen in the Chilbolton PPI Doppler scans in Fig.8 (a,c). Close inspection of the corresponding reflectivity scans (Figs.8(b,d)) shows that the apparently 2-D portions of each line segment were in fact composed of individual convective cells, each producing elongated precipitation cores orientated at a small angle to the overall line elements. This structure is typical of narrow cold-frontal rainbands due to line convection (James & Browning 1979, Hobbs and Biswas 1979) but the cells were narrow (<1km) and short (<5km), and the peak reflectivity in the line convection seldom corresponded to a rainfall intensity of more than 20 mm h^{-1} (compared with the estimated 80 mm h^{-1} in Fig.2). The anvil outflows from individual cells apparently blended together to feed the slantwise convection in S1 but, where there was a major step in the line convection, a dislocation could be seen in the resulting slantwise convection, as for example at 50km range in the 0919 UTC scan shown in Fig. 7. Even so, the different segments of the line convection still contributed to this same limb of this slantwise circulation.

(iii) The second main slantwise circulation, S2, was situated 1½ to 2km below S1 (Fig.7). For most of the time it was weaker than S1 (at least over southern England) and, whereas S1 had its roots at 2km at the top of the line convection, S2 had its roots at 1km and it was difficult to discern evidence of line convection (L2) feeding it. There were occasional line-echo patterns in the radar-network display where L2 might have been expected to be, but this evidence was untrustworthy and often attributable to bright-band artefacts. The best evidence of any L2 line convection is in the 1919 UTC scan in Fig.7 and in Fig.8(c) where the Doppler scan detects the associated divergence at about 1km. Continuity of this feature suggests that the narrow cold-frontal rainband in the northern part of the network-radar display (dashed in Fig.5(d)) is due to L2; evidently the line convection associated with L2 was more vigorous in that part of the system.

(iv) An interpretation of the essentially 2-dimensional transverse circulations associated with both S1 and S2 is that the components of the circulations with low transverse velocity, ie rearward relative velocity (warm colours in Fig.7), were ascending rearwards as shown by the arrows in Fig.7), and the components of the circulation with high transverse velocity (dark blue) were forward-descending flows relative to the moving system. This interpretation is correct for the rearward-directed warm flows which were certainly ascending. It is not necessarily true, however, that the blue flows were descending everywhere. In many parts of the blue flows the transverse component of the flow did not greatly exceed the velocity of the system. Moreover there was no systematic evidence of negative vertical gradients of reflectivity (not shown) that might have been indicative of substantial evaporation in descending air. Perhaps the most realistic interpretation is to regard the slantwise convective circulations as being superimposed on a general background of large-scale ascent, such that the rearward-sloping flows were ascending relatively strongly whereas the underlying flows were descending only weakly or in some places not all.

5. Theoretical interpretation: the possible roles of CSI and ΔM-adjustment

We have presented detailed observations of stacked slantwise circulations transverse to a vigorous ana-cold front and we have argued that their small vertical scale is suggestive of mesoscale processes such as CSI and ΔM-adjustment. We now want to look in more detail at the evidence from the model to see whether these mesoscale circulations are indeed consistent with one or other of these mechanisms. We have shown that the mesoscale version of the Unified Model, was successful in reproducing the broader-scale structure of the cold-frontal circulations; however, its failure to represent the multiple nature of the circulations means that the inferences drawn in this section will necessarily be tentative.

(a) *CSI*

We start, in Fig.9, by examining the model's slantwise convective available potential energy (SCAPE) (Shutts 1990). For a current discussion on the utility and use of SCAPE, see Sherwood (2000) and Schultz et al (2000). Figure 9 shows the SCAPE calculated with respect to air originating at 950 mb, and rising to just 700mb (the observed mesoscale circulations were mainly below the 700mb level). It shows the output of the model at 0600 and 0900 UTC, during the period when the front was approaching and crossing Wales and southwest England, as derived from the forecast run initialized at 0000UTC. Figure 9 shows regions of SCAPE along and behind the SCF. The largest values of SCAPE are along the SCF, where they reach between 100 and 300 J kg^{-1}. This is indicative of a possible role for CSI provided that (i) the CSI is coincident with a region of saturated ascent, and (ii) it does not coexist with a region of potential instability that causes gravitational convection to develop more rapidly than and to the exclusion of slantwise convection.

To demonstrate that Requirement (i) was satisfied, we have derived Fig.10, showing a series of front-perpendicular cross-sections for 0300, 0600 and 0900 UTC. The sections at these 3 times have been chosen so as to intersect approximately the same part of the front as it travelled towards the Chilbolton radar (with a slight adjustment of position to minimise orographic contamination of the vertical velocity pattern). The plots of line-convection segments in Fig.5(d) indicated that the segments crossing Chilbolton approached from the direction of Cornwall (southwest England). The positions of two of the resulting Fig.10 cross-sections are plotted in Fig.9. The three columns in Fig.10 show θ_w (left-hand column), front-perpendicular velocity (middle column), and vertical velocity and areas of near saturation (right-hand column) for each time.

The arrows superimposed on the diagrams in Fig.10 represent the authors' inferences, taking various factors into account, as to how the model was representing the line convection and slantwise convection. The vertical part of the ascending flow, which corresponds to the line convection, is drawn at the leading edge of the cold-frontal θ_w gradient corresponding to the SCF, and it passes through a maximum in the model's resolved vertical velocity. The top of this upright ascent is drawn where the air encounters a θ_w equal to that at the base of the ascent. This flow is then shown feeding a region of slantwise ascent, the axis of which is coincident with the minimum front-perpendicular wind velocity corresponding to a maximum system-relative rearward flow. This takes it roughly along an isopleth of constant θ_w. The sharpening of the gradients in Fig.10 during the course of the forecast run may be a model artefact due to the model dynamics tightening excessively smoothed initial fields; however, the overall circulation as represented by the arrows maintains a similar configuration throughout the forecast sequence.

In order to relate the vertical circulations to the distribution of CSI, the extent of SCAPE with respect to air originating at 950mb (½ km) is shown by horizontal bars in the diagrams in the right-hand column of Fig.10. These show that the

SCAPE is collocated with the main region of moist ascent that we have associated with the line convection. This is consistent with SCAPE being a possible mechanism to account for the observed slantwise circulations. However, according to Fig.11, there is non-zero CAPE along the SCF for parcels lifted from 1000 to 700mb and, although the CAPE values are mainly less than 50 J kg^{-1}, shallow upright gravitational convection (or perhaps forced convection associated with a density current) may coexist with or prevail over the release of CSI because of its faster growth rate. The radar observations suggest that this was indeed the case for the well defined line convection, L1, but less obviously so for the poorly developed L2. Evidence was sought from operational radiosonde ascents near the front to corroborate the model's indication of weak CAPE at low levels. Only one ascent was found within 50 km of the SCF, the 1200 UTC ascent from Herstmonceux (not shown). It supported the model by indicating a very small (<¼°C) decrease in θ_w over a shallow layer at low levels (930 to 840 mb).

(b) *ΔM-adjustment*

Figure 5 gave some interesting clues as to the manner in which the slantwise circulations were established. The portions of the frontal system that crossed southern England underwent a major phase of intensification before 0800 UTC. At 0600 UTC heavy rain and line convection was evident in north-west England and Wales but southwest England was affected by outbreaks of only moderate rain with a cellular distribution characteristic of disorganised weak upright convection (Fig.5(a)). Potential instability was restricted to levels below about 1.7km (Fig.4(a)) and so the convection would have been very shallow, presumably triggered by the large-scale ascent ahead of the upper-level PV anomaly (Fig.3(d)). Then, over the ensuing hours, short segments of line convection, which could just be discerned as early as 0500 UTC, intensified. At the same time, the gaps in the surrounding echo, corresponding to rain that would have been generated by the slantwise ascent, progressively filled in. It is

possible that the slantwise ascent at this stage was already being enhanced by CSI. However, these observations suggest that the slantwise ascent was also being primed by convection, albeit very shallow convection. This may have been happening at an early stage by scattered disorganized boundary-layer convection and later by more organized but still shallow line convection. Large-scale ascent may have released the potential instability and triggered the upright convection in the first place but, once triggered, this convection might have been stimulating slantwise convection by the process of ΔM adjustment. This possibility is now examined using output from the mesoscale model. As mentioned before, too much reliance should not be placed on the very detailed behaviour of the model and so the following discussion is regarded merely as an indication of plausibility.

Figure 12 shows isopleths of absolute geostrophic momentum, M_g (thick contours) superimposed on θ^*_e, the saturated equivalent potential temperature (thin contours), at 0300 UTC for part of the cross-section in Fig.10. M_g is given by $v_g + fx$, where v_g is the component of geostrophic wind in the front-parallel direction, i.e. normal to the section in Fig.12, f is the Coriolis parameter and x is distance within this section. The precise form of this diagram depends on the orientation of the cross-section; however, analyses carried out for sections orientated at $\pm 10^\circ$ on either side show that the main conclusions drawn are not altered by such changes. The bold arrow superimposed on Fig.12 shows the ascending limb of the inferred primary mesoscale circulation exactly as in Fig.10. The dashed arrow shows approximately where, according to the observations the secondary circulation should be. The dotted line shows the upper limit of where the θ^*_e contours slope more steeply than the M_g contours, and below which the moist potential vorticity was negative (not shown). As such, the dotted line represents the upper limit of the main region of CSI (there are more patches of CSI at higher levels). The vertical parts of the bold arrows in Fig.12, corresponding to the line convection, terminate fairly close to the upper boundary of the main region of CSI. It appears that, unlike in the case studied by

Zhang et al (1992), air ascending slantwise at the top of the primary line convection (solid bold line) would be stable to CSI, while parcels in the region of slantwise ascent at the top of the secondary line convection (dashed bold line) would experience CSI for only a limited displacement. It is not easy to argue that the weakness of the CSI could be due to its ongoing release, because the model has insufficient resolution to enable it properly to release CSI. Thus CSI alone may not account for the full extent of the slantwise circulations in this case. However, ΔM-adjustment may provide a more promising explanation, as we now show.

Figure 12 shows an average M_g-value of 20 ms^{-1} for air originating below 950 mb in the region of the primary line convection (bold upright arrow). This air is then lifted by the line convection to about 800 mb, into a region with ambient M_g-values of 46 ms^{-1}. If this air were to retain its original momentum after being lifted to 800mb, its motion would be significantly subgeostrophic and it would be able to continue ascending slantwise convectively until it encounters a similar value of M_g in the environment, ie to the left of the left-hand edge of Fig.12. In reality some mixing can be expected at the lower and upper boundaries of these mesoscale circulations; indeed Browning (1995) has provided evidence that the sheared boundaries of such circulations are Richardson-number limited. This will reduce the extent of the circulations associated with ΔM-adjustment but it nevertheless seems possible that this process could account for the circulations being more extensive than would be expected from CSI alone. A similar argument can be advanced for the secondary mesoscale circulation (dashed bold arrow in Fig.12) : air with an M_g-value of about 14 m s^{-1} is lifted in upright convection initially into a region where M_g is 24 m s^{-1} so that it, too, has a subgeostrophic velocity. Figure 13 shows that the potential for ΔM-adjustment existed along much of the length of the SCF. This figure shows the difference between the magnitude of the geostrophic wind velocity at the base and top of the upright convection as diagnosed from the model's parametrised convection. The predominant contribution to the geostrophic wind vector is from the front-

parallel component, v_g, and so the field plotted in Fig.13 is a useful indicator of ΔM_g.

In conclusion, therefore, we propose that the multiple mesoscale slantwise circulations may owe their existence in part to the lines of shallow upright convection and the resulting ΔM-adjustment as described by Holt and Thorpe (1991). This begs the question as to what triggers the upright convection in the first place. Presumably the primary line of upright convection could be triggered initially by the larger-scale frontogenetic circulation and then perhaps sustained by a circulation enhanced by the slantwise convection. The secondary circulation, on the other hand, is perhaps more likely to begin as a weak CSI-induced slantwise circulation that triggers upright convection which in turn strengthens the slantwise circulation intermittently via ΔM-adjustment. This is of course highly speculative since it is based partly on the interpretation of output from a NWP model which is beginning to become untrustworthy at these small scales, and so these issues need to be studied using an idealized modelling approach. It is hoped that the careful observational analysis of this case, as summarized in Section 4, will help in defining a well-posed modelling experiment. If the hypothesis that ΔM-adjustment plays an important role turns out to be valid, it would imply the need for parametrised convection in NWP models to transport upwards not only heat and moisture but also momentum.

Acknowledgements

We are grateful to A. Openshaw (Univ. of Reading) and RAL staff at Chilbolton for work enabling the acquisition of the microwave radar data, to J. Nash, T. Oakley and C. Gafford (Met. Office) for provision of high-resolution UHF radar data, and to P. Panagi and E. Dicks (Univ. of Reading) for supporting the accessing and analysis of Unified Model data. The paper has benefitted from helpful comments from P. Clark and S.L.Gray. The research brings together work

supported by the Met. Office under contract agreements Met 1b/2617, PB/B3241 and PB/B3010, and by the Natural Environment Research Council under contract DST 26/39. The Joint Centre for Mesoscale Meteorology itself is supported by the Met Office and the Department of Meteorology, University of Reading, and by NERC through its support of the Universities Weather Research Network, UWERN.

References

Bennetts, D.A. and Hoskins B.J. 1979 Conditional symmetric instability – a possible explanation for frontal rainbands *Q.J.R.Meteorol.Soc.*, **105,** 945-962

Browning, K.A. 1990 Organisation of clouds and precipitation in extratropical cyclones. Pp129-153 in *Extratropical cyclones*. Eds. C.W. Newton and E.O. Holopainen, American Meteorological Society, Boston, Mass

Browning, K.A. 1995 On the nature of the mesoscale circulations at a kata-cold front, *Tellus*, **47A,** 911-919

Browning, K.A. and Harrold, T.W. 1970 Air motion and precipitation growth at a cold front. *Q.J.R.Meteorol.Soc.*, **96,** 369-389

Browning, K.A. and Pardoe, C.W. 1973 Structure of low-level jet streams ahead of mid-latitude cold fonts, *Q.J.R.Meteorol.Soc.*, **99,** 619-638

Browning,K.A., Roberts, N.M. and Illingworth, A.J. 1997 Mesoscale analysis of the activation of a cold front during cyclogenesis, *Q.J.R.Meteorol.Soc., **123,** 2349-2375*

Dixon, R.S. 2000 Diagnostic studies of symmetric instability, PhD Thesis, University of Reading.

Emanuel, K.A. 1994 *Atmospheric convection*, Oxford University Press.

Fischer, C, and Lalaurette,F. 1995 Meso-β-scale circulations in realistic fronts.II: Frontogenetically forced basic states. *Q.J.R.Meteorol.Soc.*, ***121,***1285-1321

Goddard, J.W.F., Eastment, J.D. and Thurai, M. 1994 The Chilbolton advanced meteorological radar: a tool for multidisciplinary research *Electronics and Communications Engineering Journal,* **6,** 77-86

Gray, S.L., Craig, G.C. and Browning, K.A. 2000 UK mesoscale modelling strategy: an outline implementation plan. Joint Centre for Mesoscale Meteorology Internal Report.

Hobbs, P.V. and Biswas, K.R.1979 The cellular structure of narrow cold–frontal rainbands. *Q.J.R.Meteorol.Soc.*, **105,** 723-727

Holt, M.W. and Thorpe, A.J. 1991 Localized forcing of slantwise motion at fronts. *Q.J.R.Meteorol.Soc.*, **117,** 943-963

James, P.K. and Browning, K.A. 1979 Mesoscale structure of line convection at surface cold fronts. *Q.J.R.Meteorol.Soc.*, **105,** 371-382

Lhermitte, R.M. and Atlas, D. 1961 Precipitation motion by pulse Doppler. In *Proc.Ninth Weather Radar Conf,* pp.218-223, Amer.Meteorol.Soc., Boston, Mass

Met Office 1997 Source Book to the Forecasters' Reference Book. Met.O. 1024. Meteorological Office College, February 1997

Persson, P.O.G. and Warner, T.T. 1993 Nonlinear hydrostatic conditional symmetric instability : implications for numerical weather prediction. *Mon.Wea.Rev.*, **121**, 1821-1833

Schultz, D.M. and Schumacher, P.N. 1999 The use and misuse of conditional symmetric instability. *Mon.Wea.Rev.*, **127**, 2709-2732; Corrigendum, **128,** 1573

Schultz, D.M., Schumacher, P.N. and Doswell III, C.A. 2000 The intricacies of instabilities, *Mon.Weather.Rev*, **128**, 4143-4148

Sherwood, S.C. 2000 On moist instability, *Mon.Weather.Rev*, **128**, 4139-4142

Shutts, G.J. 1990 SCAPE charts from numerical weather prediction forecasts. *Mon.Wea.Rev.*, **118**, 2745-2751

Wakimoto, R.M. and Bosart, B.L. 2000 Airborne radar observations of a cold front during FASTEX. *Mon.Weather Rev.*, **128,** 2447-2470

Xu, Q. 1986 Conditional symmetric instability and mesoscale rainbands. *Q.J.R.Meteorol.Soc.*, **112**, 315-334

Zhang, D-L. and Cho, H-R. 1992 The development of negative moist potential vorticity in the stratiform region of a simulated squall line. *Mon.Weather.Rev.*, **120**, 1322-1341

Figure legends

Fig.1. Conceptual model of the airflow at a classical ana-cold front showing air in the warm conveyor belt undergoing rearward-sloping ascent (bold arrow) above the cold-frontal zone, with cold air (dashed lines) undergoing forward-sloping descent beneath it. Flows are shown relative to the frontal system, moving from left to right. The broken-hatched shading represents precipitation falling beneath the base of layer cloud, shown stippled. (From Browning 1990).

Fig.2. Cross-section showing airflow transverse to an intense ana-cold front, obtained using the Chilbolton Doppler Radar at 1839 UTC on 24 Oct 1995 (from Browning et al 1997). The frontal system was travelling from left to right. The colours denote system-relative Doppler velocity according to the scale. Black lines are streamlines derived from the Doppler velocities assuming 2-dimensional flow.

Fig.3. Plan depictions of the frontal system at 0900 UTC, 10 February 2000. Panels (a), (c) and (d) are T+3 forecasts from the mesoscale version of the Unified Model and (b) is the Meteosat infra-red image for the corresponding area. The dashed line in (a) delineates the area of cold (high) cloud in (b) that was associated with the main cold-frontal ascent. Panel (c) gives 900-mb θ_w , with contours at 1 °C intervals (shaded > 7 °C). Panel (d) gives the height of the PV=2 PV units surface in kilometres (shaded < 10km). The contours within 1 deg of the bottom and right-hand boundaries of (d) are model artefacts and should be disregarded. The orientation of the model and radar cross-sections shown in Figs.4 and 7, is given by the line XX in (a) and the position of the Chilbolton radar within the section is denoted by the black spot.

Fig.4. Cross-sections, along XX in Fig.3(a), through the frontal system at 0900 UTC, 10 February 2000, derived from T+3 forecasts from the mesoscale version of the Unified Model : (a) θ_w at 1 °C intervals (shaded > 8 °C), (b) PV at 0.5 unit intervals from 0 to 2 units (shaded > 1 unit), (c) front-parallel wind component at 4 ms^{-1} intervals, (d) front-perpendicular wind component at 2 ms^{-1} intervals (shaded < 16 ms^{-1}), and (e) relative humidity with respect to ice at 5% intervals (shaded > 95%). Aspects of (a) – (e) have been extracted and plotted together in (f) : see text for details. (Although the distance scales are labelled for simplicity as north-west to south-east, they are strictly along 309 to 129° to correspond to the radar sections in Fig.7. The wind components in (c) and (d) are from 039° and 309°, respectively, again to correspond to the velocities in the radar sections in Fig.7: this direction is close to the front-perpendicular direction of 300°).

Fig.5. Radar-network pictures showing surface rainfall distributions at (a) 0600UTC, (b) 0800 UTC and (c) 1000 UTC, 10 February 2000. Panel (d) shows successive hourly positions of the line convection responsible for the dominant narrow cold-frontal rainband (L1 solid, L2 dashed), as derived from (a), (b), (c) and other pictures in this sequence. (Bands of intense (red) echo towards the rear edge of the rain area in the southern half of the pictures are due in part to bright-band effects and so are not represented in (d)). Also shown in (d) are the locations of the radar wind profilers at Camborne(*) and Dunkerswell (x) and the microwave Doppler radar at Chilbolton (+ and a 95 km radius circle indicating radar coverage).

Fig.6. Time-height sections of wind components (a,c) parallel and (b,d) perpendicular to the front. (a) and (b) are 15-minute averages of 5-minute data from the UHF wind profiler at Camborne (* in Fig.5), with hatching where data are missing due to low signal. Contours are at 2 m s^{-1} intervals

with shading according to the key (in m s^{-1}) on the right-hand side. The solid and dashed arrows in (b) indicate the circulations S1 and S2, respectively. (c) and (d) are the corresponding wind components derived from hourly output of a forecast from the the mesoscale version of the Unified Model, initialised at 0000 UTC for the grid point nearest to Camborne. The system velocity is 16 m s^{-1} and wind components less than this (dark shading in (b) and (d)) correspond to rearward-directed flows relative to the front.

Fig.7. Eight RHI scans from the Chilbolton radar showing Doppler velocity within vertical sections almost normal to the front at 0822 (bottom), 0851, 0919, 0948, 1005, 1016, 1033, and 1112 UTC (top) on 10 February 2000. Most of the RHIs were obtained towards 309°; those at 1005, 1033 and 1112 UTC were obtained towards 129°. Velocities (relative to the ground) are given by the colour code, with positive velocities consistently being from left to right. The principal layers of slantwise ascent, S1 and S2, are shown by the continuous and dashed lines, respectively, the direction of these flows being indicated relative to the moving frontal system. (The dotted line shows another layer of rearward relative flow which existed ahead, i.e. independently, of L1).. The main layers, S1 and S2, are fed by almost upright line convection, L1 and L2. The RHIs are displaced laterally according to the system velocity so that the position of L1 is aligned along the vertical dotted line.

Fig.8 (a-d) show two PPI scans at elevation 1.0° from the Chilbolton radar at (a,b) 0827-0833 UTC and (c,d) 0924 – 0930 UTC on 10 February 2000. Scans were made anticlockwise starting at north. The left column (a,c) shows Doppler velocity in m $^{s-1}$ according to the colour scales: positive velocities are towards the radar. The right-hand column (b,d) shows reflectivity in dBz. The full radar range (5 to 95 km) is shown for the Doppler velocity displays. The reflectivity plots in (b) and (d) are for enlarged parts of the

velocity displays as shown by the superimposed boxes in (a) and (c), respectively. Locations of the line convection (two segments associated with L1 and one with L2) are highlighted by dotted lines in the velocity displays. Panels (e) and (f) show velocity data obtained with the Chilbolton radar between 1130 and 1133 UTC: (e) is part of a PPI scan at 1.5° elevation showing Doppler velocity, and (f) is the corresponding wind hodograph, with crosses showing wind vectors at 0.25 km height intervals from 1 to 3km. The dashed lines in (f) show the orientation of the front which was travelling at 16 ms^{-1} (blue arrow). S1 and S2 label the rearward-sloping branches of the two main slantwise circulations, which are characterised by local minima in the wind component away from the radar, ie maxima in front-relative rearward velocity.

Fig. 9 SCAPE for air lifted from 950 mb to 700 mb at (a) 0600 UTC and (b) 0900 UTC on 10 February 2000, derived from the output of the forecast from the mesoscale version of the Unified Model initialised at 0000 UTC. Isopleths of SCAPE are for 30 and 100 J kg^{-1} (shaded over 100 J kg^{-1}). Lines indicate the positions of cross-sections shown in Fig. 10.

Fig.10 Wet-bulb potential temperature, θ_w, (left-hand column), front-perpendicular velocity (middle column), and vertical velocity and relative humidity (right-hand column) at 0300 UTC (top row), 0600 UTC (middle row) and 0900 (bottom row) on 10 February 2000, within the cross-sections through the cold front shown in Fig.9, as derived from the output of the forecast from the mesoscale version of the Unified Model initialised at 0000 UTC. Isopleths of θ_w are shown at 1°C intervals, isopleths of front-perpendicular velocity are at 2 m s^{-1} intervals (shading represents flow rearwards relative to the 16 m s^{-1} velocity of the front) and isopleths of vertical velocity are at 2 cm s^{-1} intervals, with shading where relative humidity exceeds 95%. The horizontal bar at height ½km in the right-hand column represents the horizontal extent of air at 950 mb

with positive SCAPE. The arrows in each panel are a schematic representation of the model's transverse circulation (in a given row the arrows are the same for each panel).

Fig.11 Same as Fig.9 but showing CAPE for air lifted from 1000 mb to 700 mb, with isopleths at 10, 30 and 100 J kg^{-1}.

Fig.12 M_g surfaces (thick lines at intervals of 4 m s^{-1}) and saturated equivalent potential temperature, θ^*_e, (thin lines at 1°C intervals) at 0300 UTC on 10 February 2000, for part of the cross-section in Fig.10 (top row), derived from the output of the forecast from the mesoscale version of the Unified Model initialised at 0000 UTC. The solid and dashed arrows represent the inferred approximate locations of the ascending parts of the two observed mesoscale circulations.

Fig.13 Same as Fig. 9 but showing the difference between the magnitude of the geostrophic wind velocity at the base and top of the upright convection as diagnosed from the model's parametrised convection. Isopleths are for 10 and 20 m s^{-1} (shaded over 20 m s^{-1}).

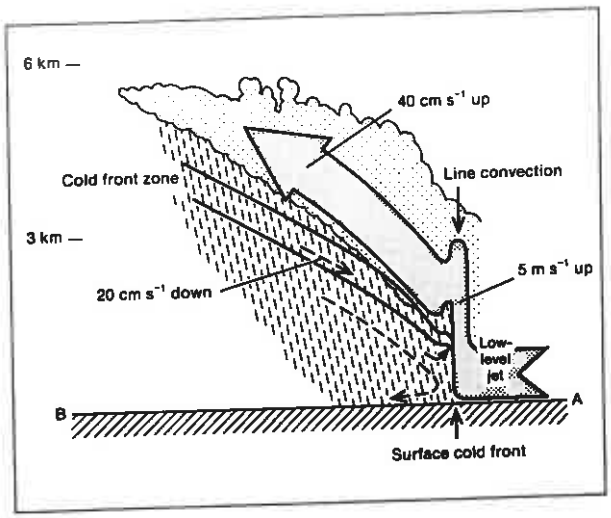
6 km
3 km
40 cm s⁻¹ up
Line convection
Cold front zone
5 m s⁻¹ up
20 cm s⁻¹ down
Low-level jet
B
A
Surface cold front

Fig. 1

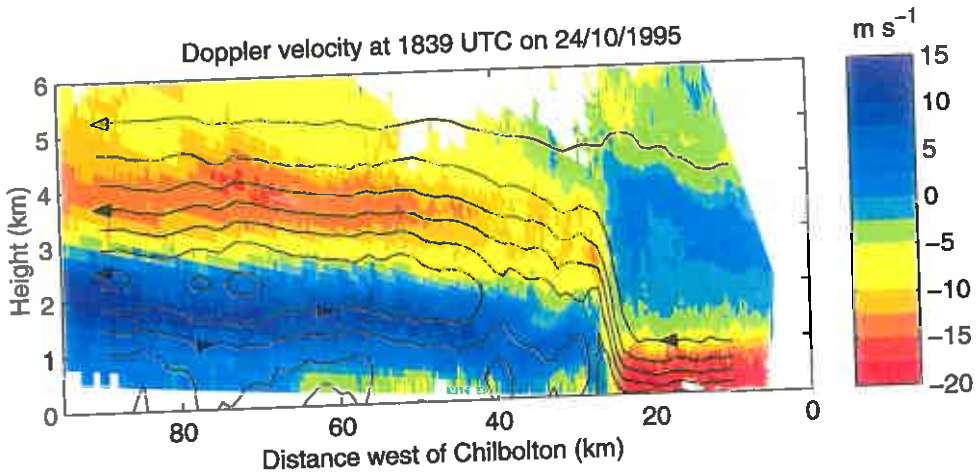
Doppler velocity at 1839 UTC on 24/10/1995
m s^{-1}
15
10
5
0
−5
−10
−15
−20
Height (km)
0
1
2
3
4
5
6
80
60
40
20
0
Distance west of Chilbolton (km)

Fig. 2

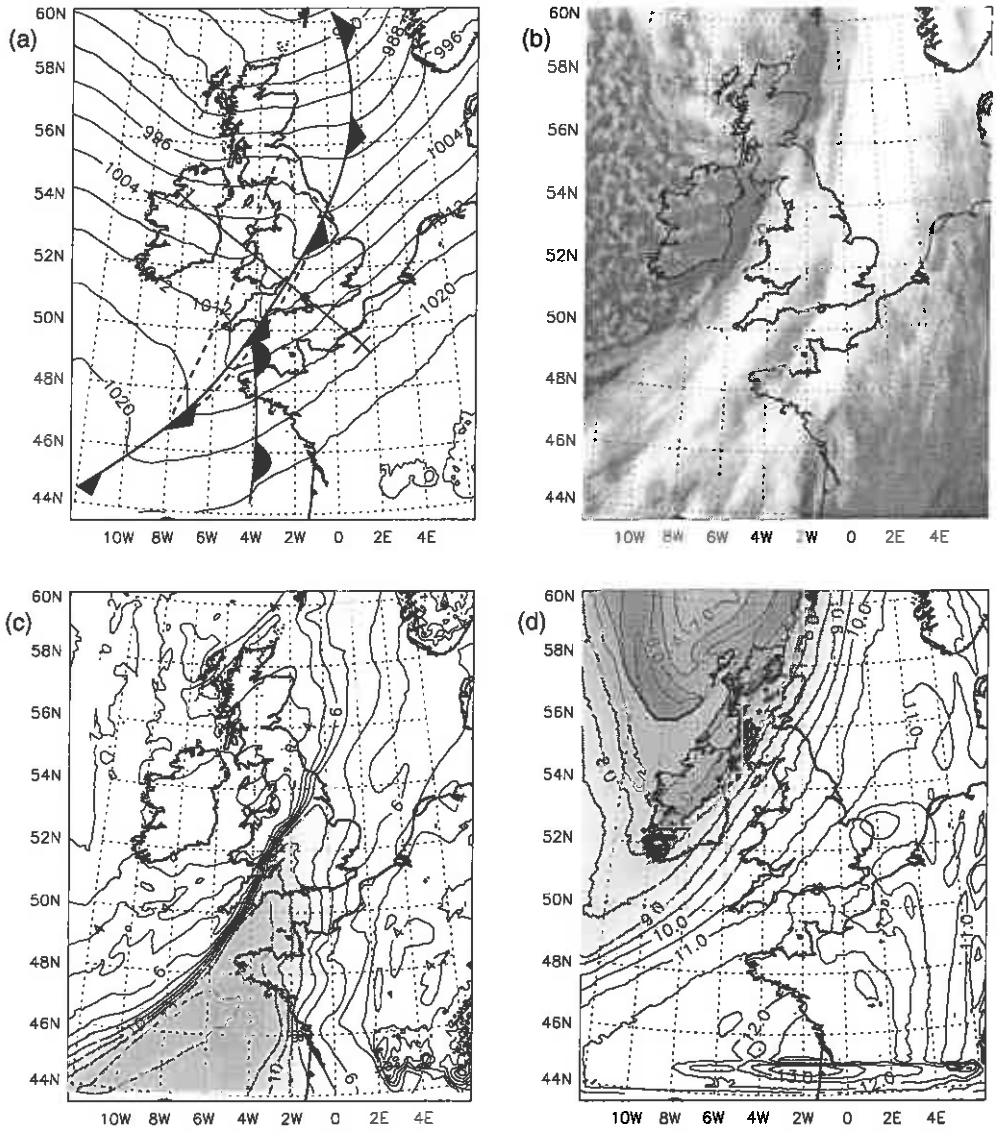
(a)
(b)
(c)
(d)
60N
58N
56N
54N
52N
50N
48N
46N
44N
10W 8W 6W 4W 2W 0 2E 4E
1004
1012
1020
996
988
9.0
10.0
11.0
12.0
13.0

Fig. 3

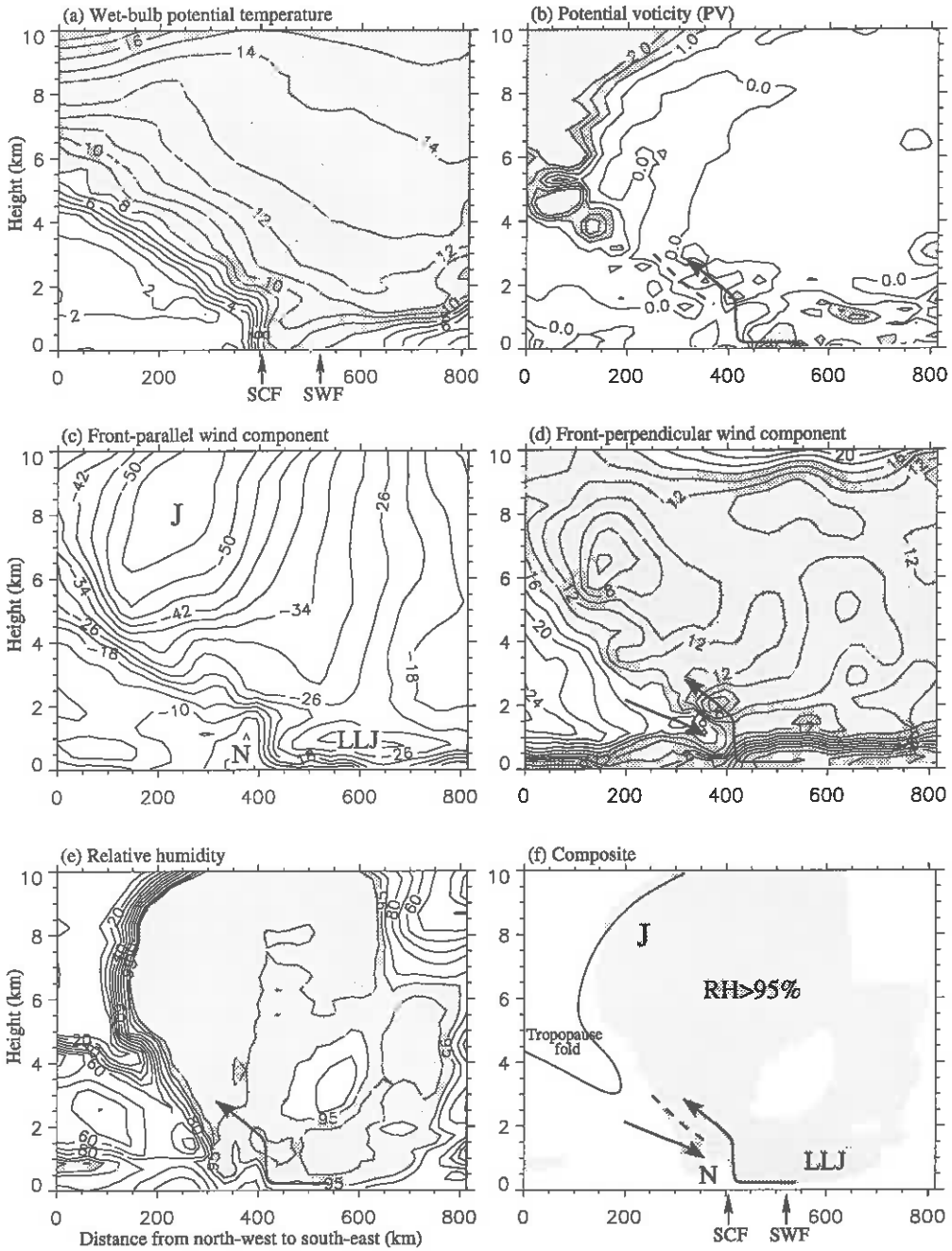
(a) Wet-bulb potential temperature
(b) Potential voticity (PV)
(c) Front-parallel wind component
(d) Front-perpendicular wind component
(e) Relative humidity
(f) Composite
Height (km)
Distance from north-west to south-east (km)
SCF
SWF
J
N
LLJ
RH>95%
Tropopause fold

Fig. 14

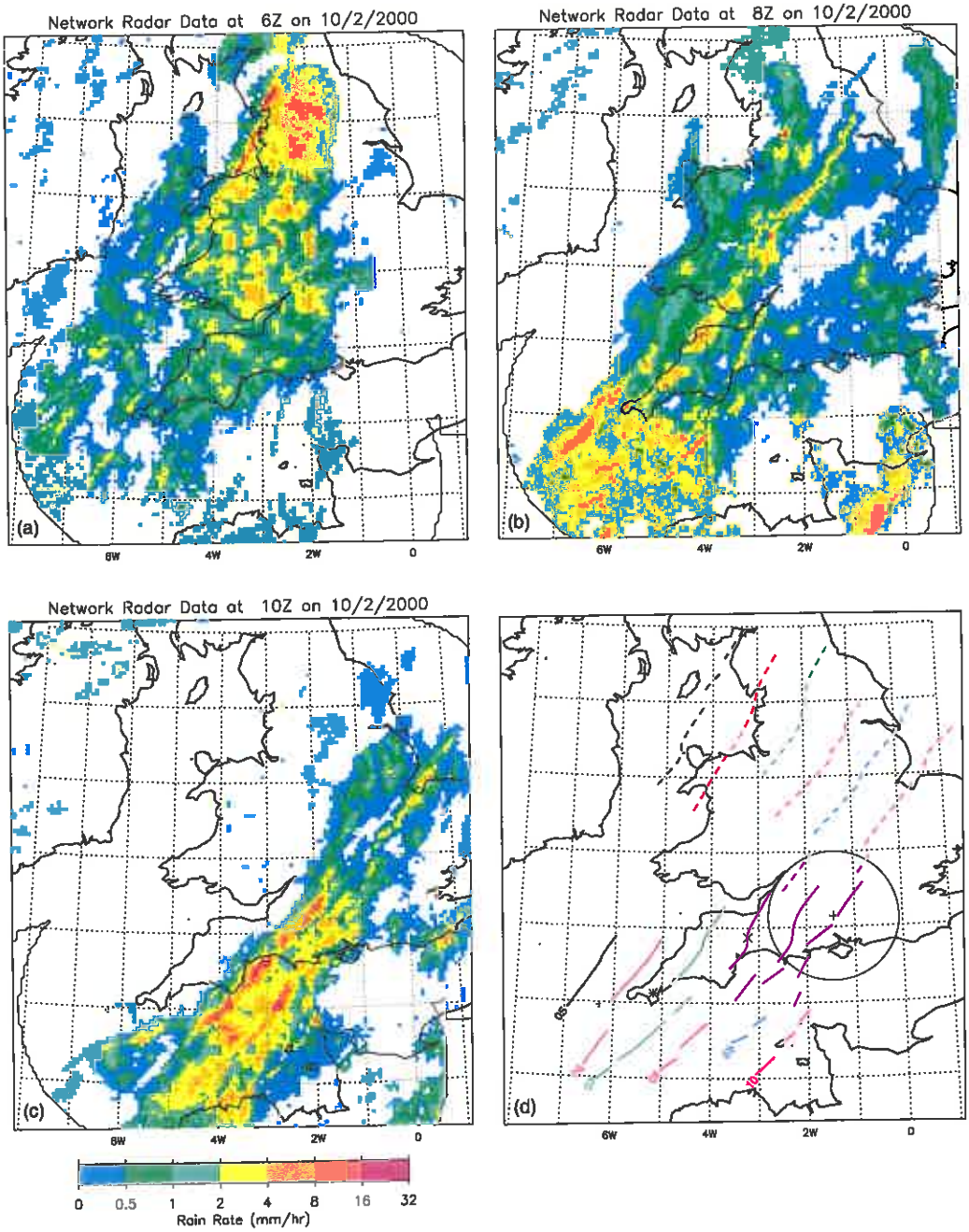
Network Radar Data at 6Z on 10/2/2000
Network Radar Data at 8Z on 10/2/2000
Network Radar Data at 10Z on 10/2/2000
(a)
(b)
(c)
(d)
6W
4W
2W
0
0
0.5
1
2
4
8
16
32
Rain Rate (mm/hr)

Fig. 5

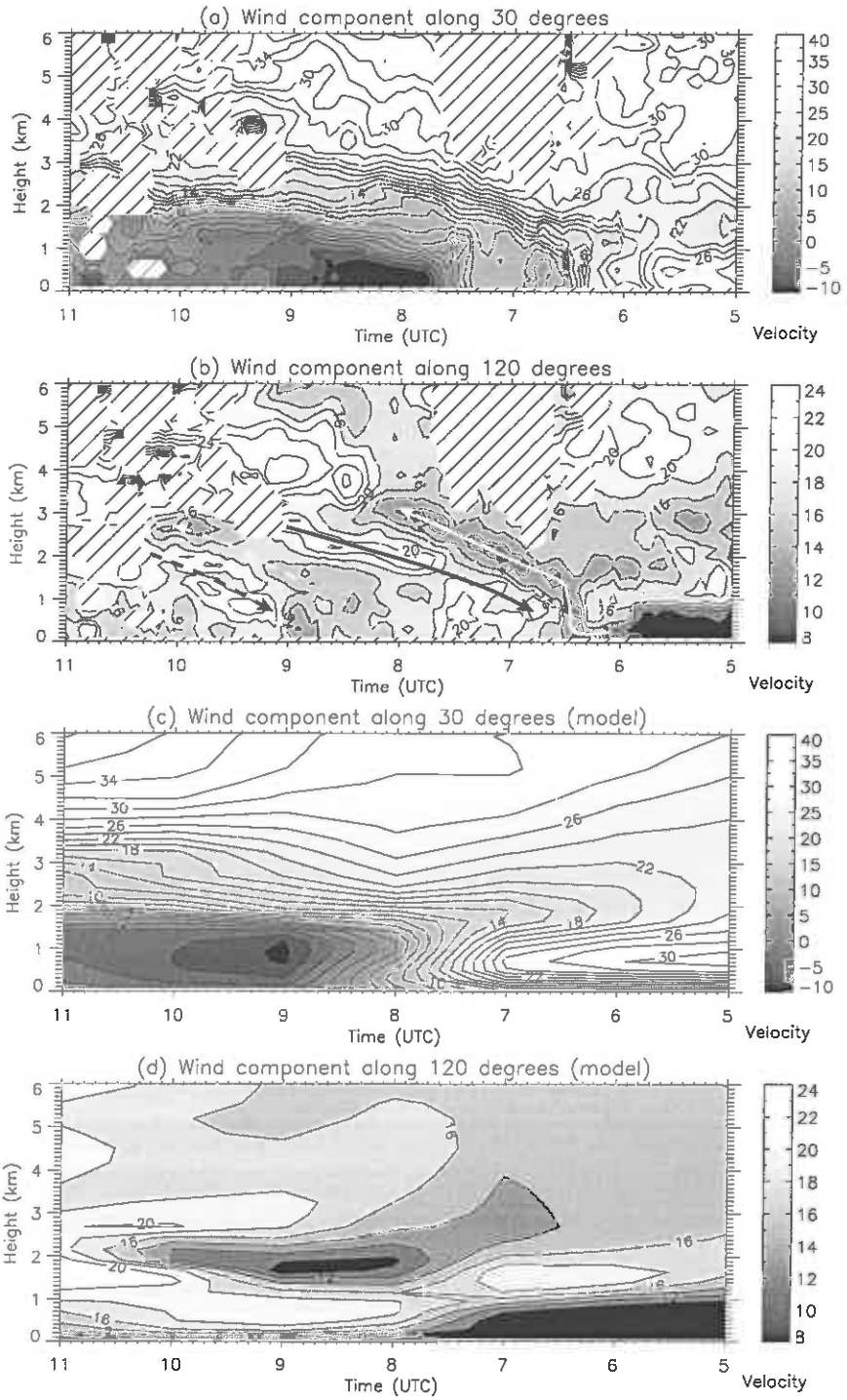
(a) Wind component along 30 degrees
Height (km)
Time (UTC)
Velocity
(b) Wind component along 120 degrees
Height (km)
Time (UTC)
Velocity
(c) Wind component along 30 degrees (model)
Height (km)
Time (UTC)
Velocity
(d) Wind component along 120 degrees (model)
Height (km)
Time (UTC)
Velocity

Fig. 6

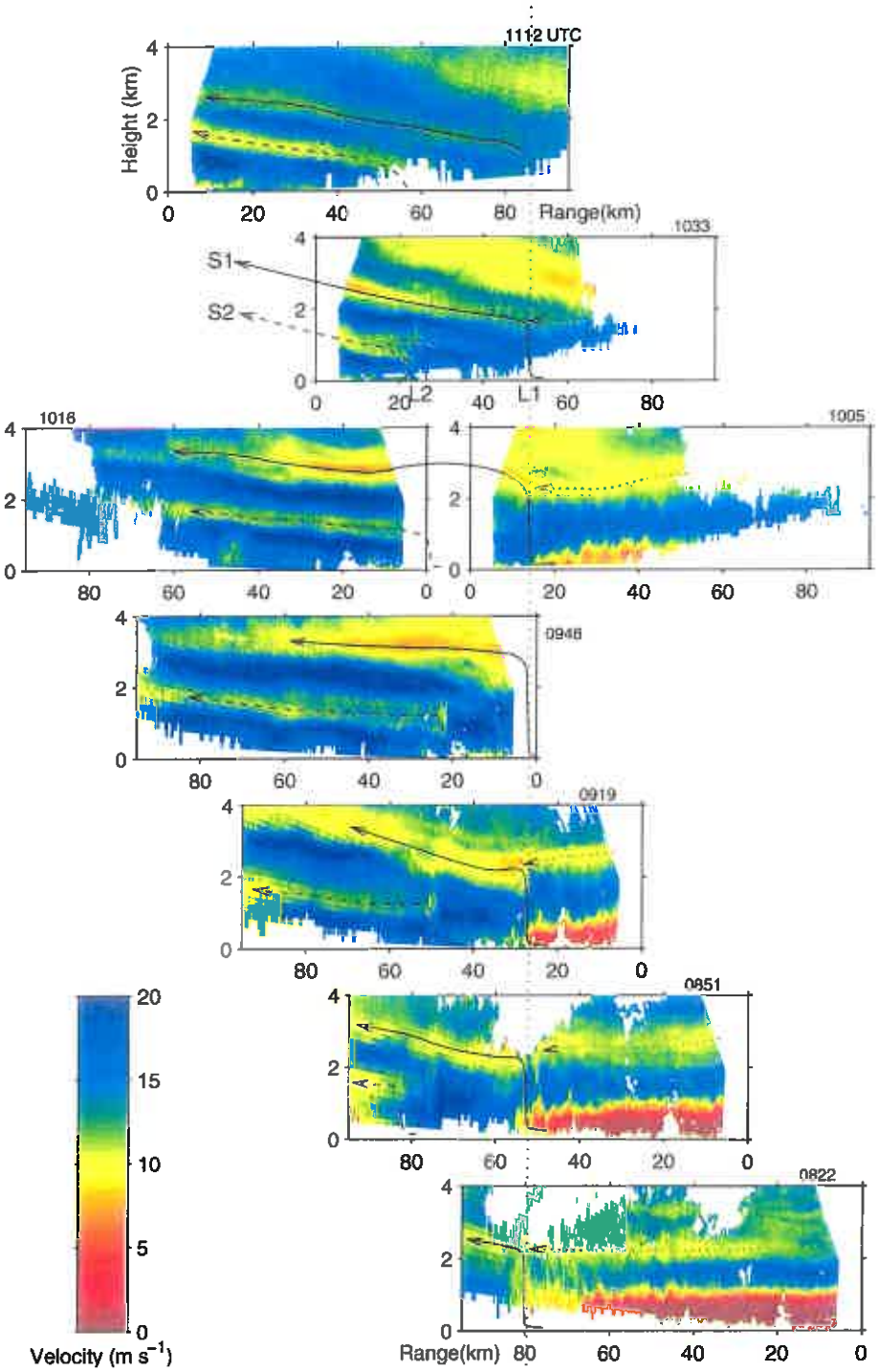
1112 UTC
Height (km)
Range(km)
1033
S1
S2
L2
L1
1016
1005
0948
0919
0851
0822
Velocity (m s^{-1})

Fig 7

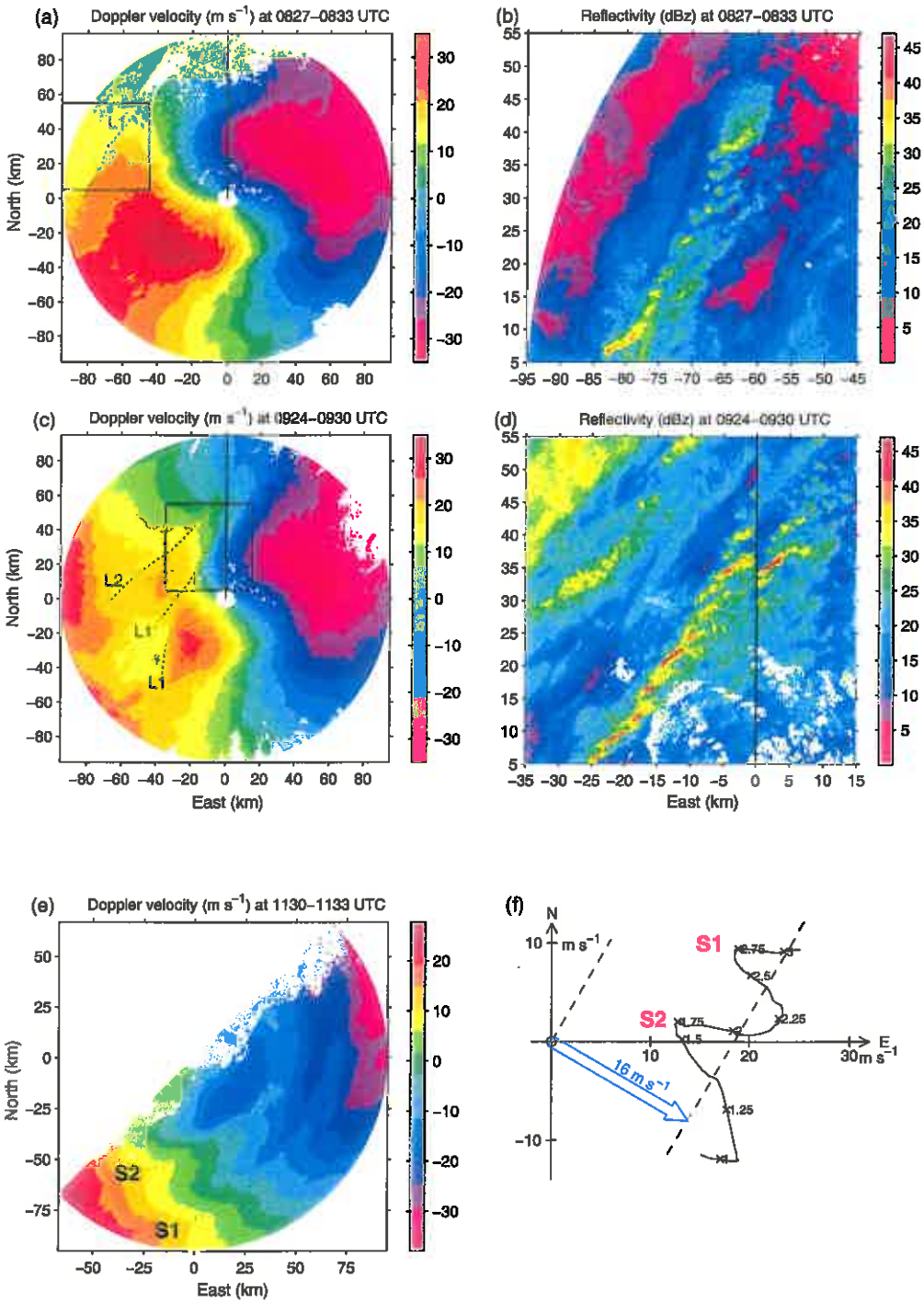
(a) Doppler velocity (m s^{-1}) at 0827–0833 UTC
(b) Reflectivity (dBz) at 0827–0833 UTC
(c) Doppler velocity (m s^{-1}) at 0924–0930 UTC
(d) Reflectivity (dBz) at 0924–0930 UTC
(e) Doppler velocity (m s^{-1}) at 1130–1133 UTC
(f)
North (km)
East (km)
L1
L2
S1
S2
N
E
10 m s^{-1}
30 m s^{-1}
16 m s^{-1}

Fig. 8

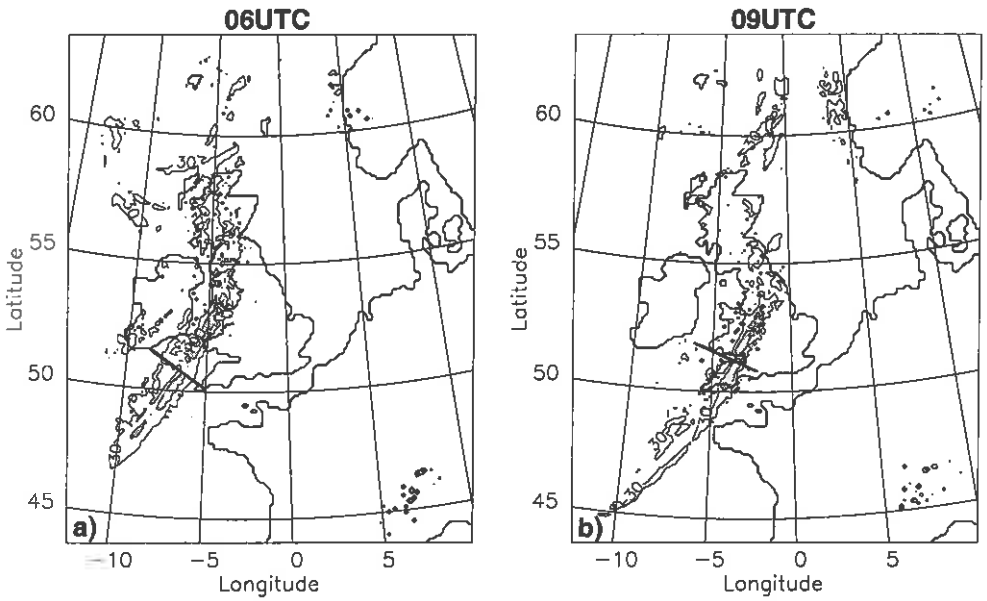

Fig. 9

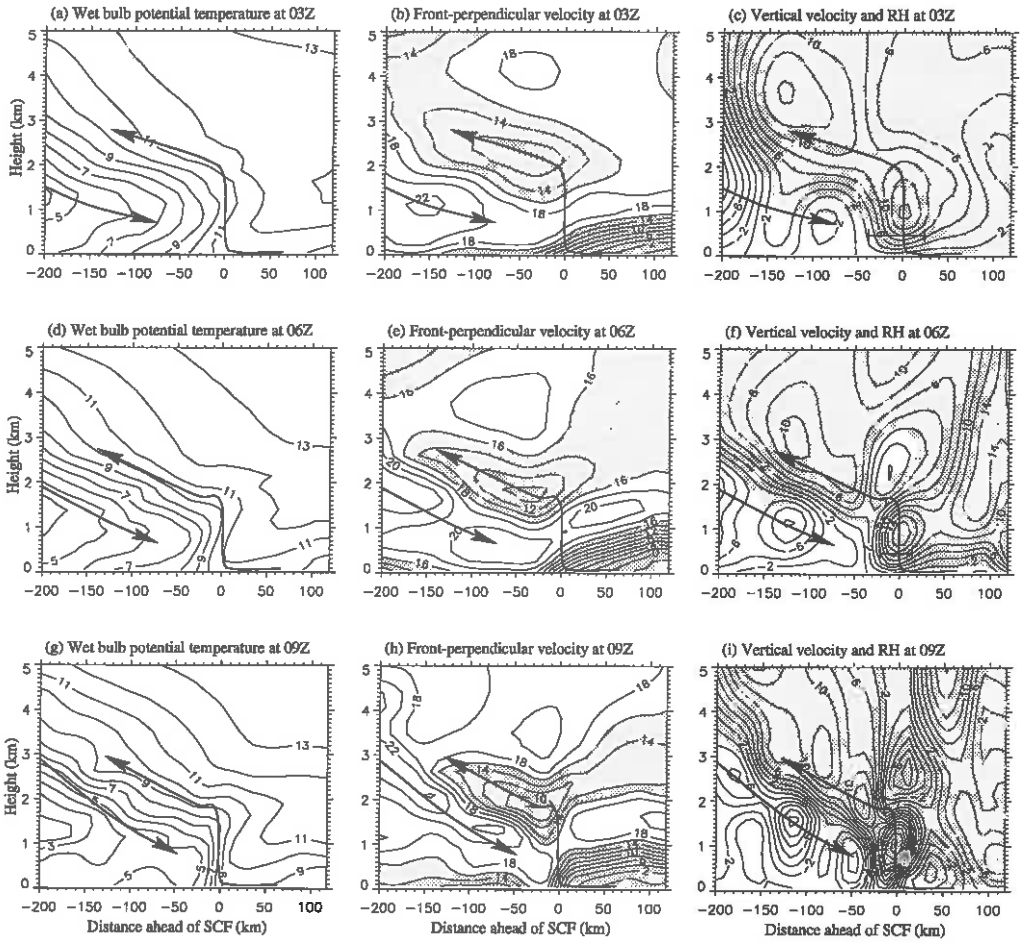
(a) Wet bulb potential temperature at 03Z
(b) Front-perpendicular velocity at 03Z
(c) Vertical velocity and RH at 03Z
(d) Wet bulb potential temperature at 06Z
(e) Front-perpendicular velocity at 06Z
(f) Vertical velocity and RH at 06Z
(g) Wet bulb potential temperature at 09Z
(h) Front-perpendicular velocity at 09Z
(i) Vertical velocity and RH at 09Z
Height (km)
Distance ahead of SCF (km)

Fig. 10

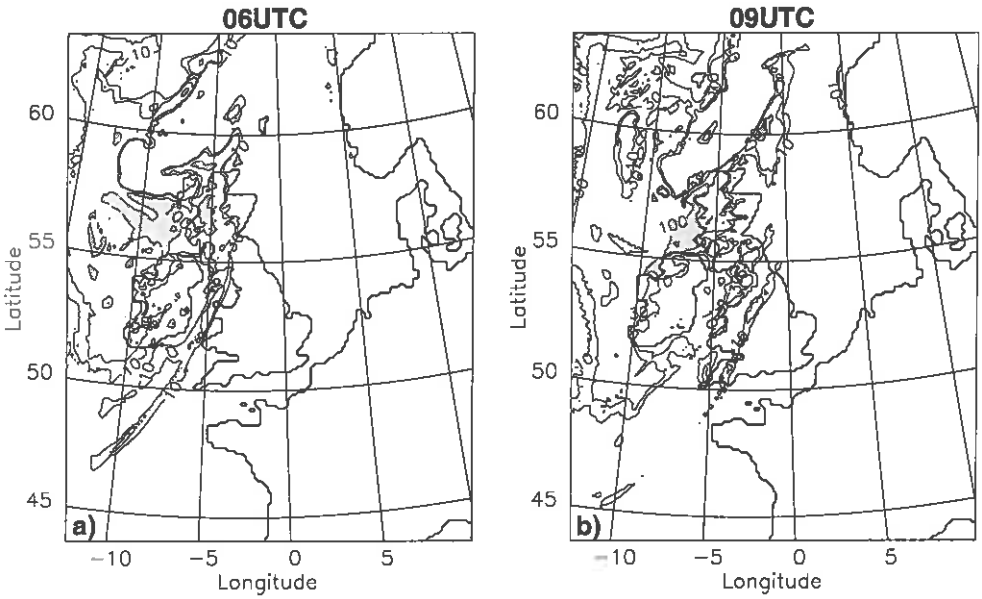

Fig. 11

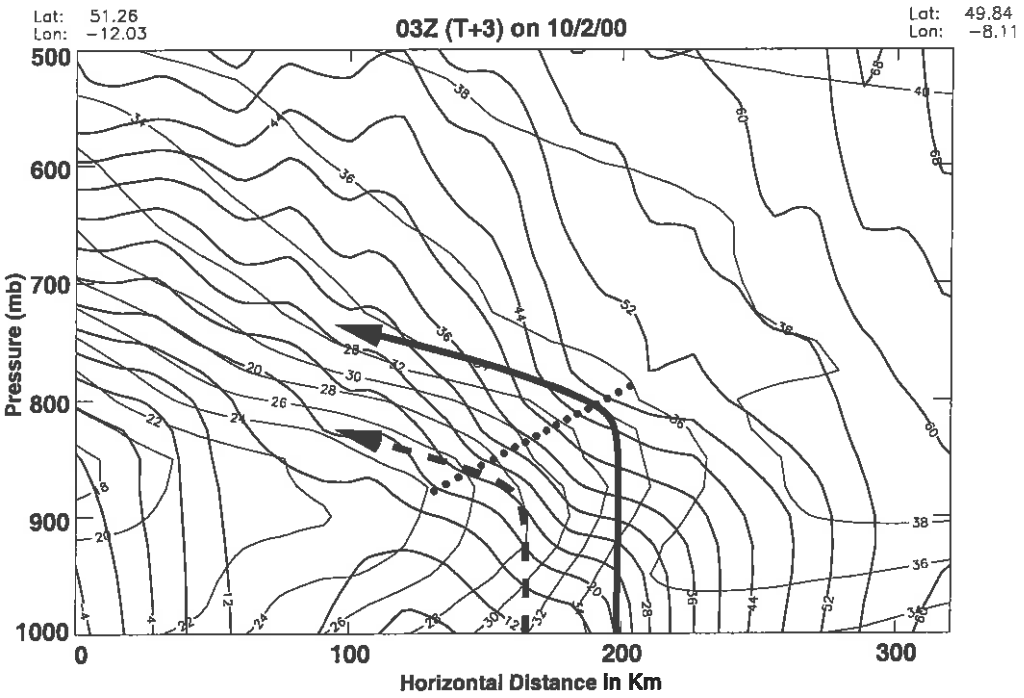
Lat: 51.26
Lon: −12.03
03Z (T+3) on 10/2/00
Lat: 49.84
Lon: −8.11
Pressure (mb)
500
600
700
800
900
1000
0
100
200
300
Horizontal Distance in Km

Fig. 12

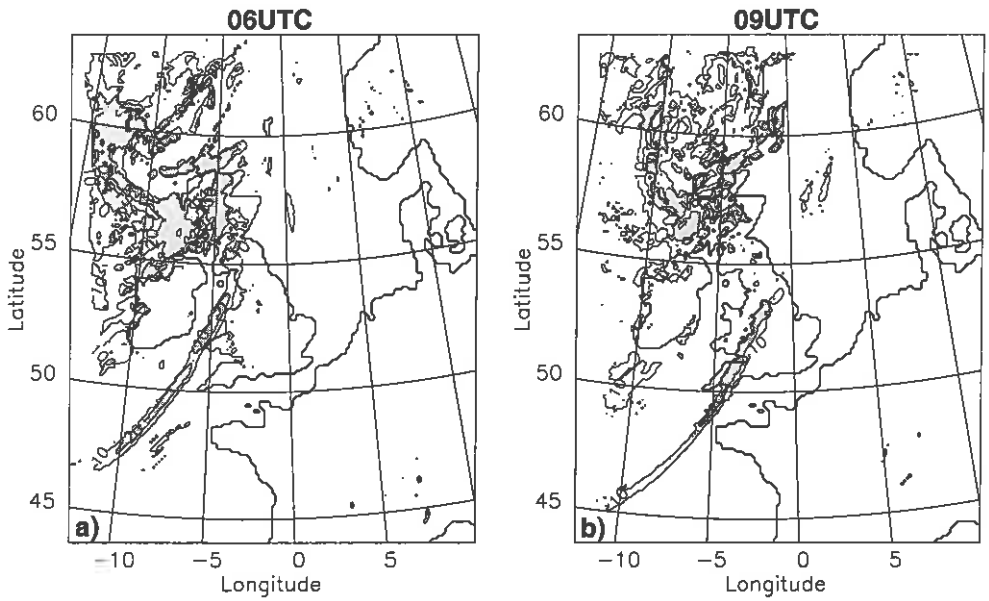

Fig. 13

CURRENT JCMM INTERNAL REPORTS

This series of JCMM Internal Reports, initiated in 1993, contains unpublished reports and also versions of articles submitted for publication. The complete set of Internal Reports is available from the National Meteorological Library on loan, if required.

1. **Research strategy and programme**
   K A Browning et al
   January 1993

2. **The GEWEX Cloud System Study (GCSS)**
   GEWEX Cloud System Science Team
   January 1993

3. **Evolution of a mesoscale upper tropospheric vorticity maximum and comma cloud from a cloud-free two dimensional potential vorticity anomaly**
   K A Browning
   January 1993

4. **The global energy and water cycle**
   K A Browning
   July 1993

5. **Structure of a midlatitude cyclone before occlusion**
   K A Browning and N Roberts
   July 1993

6. **Developments in systems and tools for weather forecasting**
   K A Browning and G Szejwach
   July 1993

7. **Diagnostic study of a narrow cold frontal rainband and severe winds associated with a stratospheric intrusion**
   K A Browning and R Reynolds
   August 1993

8. **Survey of perceived priority issues in the parametrizations of cloud-related processes in GCMs**
   K A Browning
   September 1993

9. **The effect of rain on longwave radiation**
   I Dharssi
   September 1993

10. **Cloud microphysical processes - a description of the parametrization used in the large eddy model**
    H Swann
    October 1993

11. **An appreciation of the meteorological research of Ernst Kleinschmidt**
    A J Thorpe
    May 1992

12. **Potential vorticity of flow along the Alps**
    A J Thorpe, H Volkert and Dietrich Heimann
    August 1992

13. **The representation of fronts**
    A J Thorpe
    January 1993

14. **A parametrization scheme for symmetric instability: test for an idealised flow**
C S Chan and A J Thorpe
February 1993

15. **The Fronts 92 Experiment: a Quicklook Atlas**
Edited by T D Hewson
November 1993

16. **Frontal wave stability during moist deformation frontogenesis**
Part 1: Linear wave dynamics
C H Bishop and A J Thorpe
May 1993

17. **Frontal wave stability during moist deformation frontogenesis**
Part 2. The suppression of non-linear wave development
C H Bishop and A J Thorpe
May 1993

18. **Gravity waves in sheared ducts**
S Monserrat and A J Thorpe
October 1993

19. **Potential vorticity and the electrostatics analogy: quasi-geostrophic theory**
C Bishop and A J Thorpe
November 1993

20. **Recent advances in the measurement of precipitation by radar**
A J Illingworth
April 1993

21. **Micro-physique et givrage: cloud microphysics and aircraft icing**
A J Illingworth
May 1993

22. **Differential phase measurements of precipitation**
M Blackman and A J Illingworth
May 1993

23. **Estimation of effective radius of cloud particles from the radar reflectivity**
N I Fox and A J Illingworth
May 1993

24. **A simple method of Dopplerising a pulsed magnetron radar**
A Hua, A J Illingworth and J Eastment
November 1993

25. **Radiation and polar lows**
George C Craig
February 1994

26. **Collected preprints submitted to the International Symposium on the Life Cycles of Extratropical Cyclones; Bergen, Norway, 27 June - 1 July 1994**
April 1994

27. **Convective frontogenesis**
Douglas J Parker and Alan J Thorpe
April 1994

28. **Improved measurement of the ice water content in cirrus using a total water evaporator**
Philip R A Brown and Peter N Francis
April 1994

29. **Mesoscale effects of a dry intrusion within a vigorous cyclone**
K A Browning and B W Golding
April 1994

30. **GEWEX Cloud System Study, Science Plan**
May 1994

31. **Parametrization of momentum transport by convectively generated gravity waves**
R Kershaw
May 1994

32. **Mesoscale Modelling Newsletter No 5**
May 1994

33. **Observations of the mesoscale sub-structure in the cold air of a developing frontal cyclone**
K A Browning, S A Clough, C S A Davitt, N M Roberts and T D Hewson
May 1994

34. **Longwave radiative forcing of a simulated tropical squall line**
Imtiaz Dharssi
July 1994

35. **On the nature of the convective circulation at a kata-cold front**
K A Browning
September 1994

36. **Collective preprints of papers submitted to the COST-75 International Seminar on Advanced Weather Radar Systems, Brussels, 20-23 September 1994**
November 1994

37. **Use of satellite imagery to diagnose events leading to frontal thunderstorms: Parts I and II of a case study**
K A Browning and N M Roberts
November 1994

38. **The role of spaceborne millimetre-wave radar in the global monitoring of ice cloud**
P R A Brown, A J Illingworth, A J Heymsfield, G M McFarquhar, K A Browning and M Gosset
December 1994

39. **Potential vorticity inversion**
Michal Ziemianski
October 1994

40. **Theory of mature tropical cyclones; a comparison between Kleinschmidt (1951) and Emanuel (1986)**
Suzanne L Gray
December 1994

41. **Dispersion and removal of pollutants during the passage of an atmospheric frontal system**
N R Gimson
December 1994

42. **The role of snow sublimation in frontogenesis**
D J Parker and A J Thorpe
December 1994

43. **Potential vorticity and the electrostatics Analogy: Ertel-Rossby formulation**
A J Thorpe and C H Bishop
December 1994

44. **Mesoscale aspect of extratropical cyclones: an observational perspective**
K A Browning
January 1995

45. **A polar low outbreak: evolution and mesoscale structures**
T D Hewson, G C Craig and C Claud
February 1995

46. **Generation of near-surface gusts of deep convection**
K Nakamura and R Kershaw
April 1995

47. **Attribution concepts applied to the Omega Equation**
S A Clough, C S A Davitt and A J Thorpe
June 1995

48. **Parametrization of mixed-phase cloud and precipitation**
Susan P Ballard and M Gerard Hutchinson
June 1995

49. **Short-range forecasting of stratocumulus: initialization prediction**
Susan P Ballard, Simon D Jackson and B Macpherson
June 1995

50. **Contributions of the JCMM/Dept of Meteorology Radar Group to the 27th AMS Radar Meteorology Conference, Vail October 1995**
June 1995

51. **Cold pools in shear**
Douglas J Parker
September 1995

52. **High-resolution analysis of frontal fracture**
K A Browning, S P Ballard and C S A Davitt
September 1995

53. **The albedo of broken cloud fields: calculations using a modified two stream radiation code**
Imtiaz Dharssi and Roy Kershaw
October 1995

54. **Parametrization of momentum transport by convection. I: theory and cloud modelling results**
R Kershaw and D Gregory
November 1995

55. **Variation of frontal structure along a cold front**
K A Browning and N M Roberts
November 1995

56. **Secondary frontal waves**
Douglas Parker
December 1995

57. **Objective fronts**
T D Hewson
March 1996

58. **Mesoscale analysis of the activation of a cold front during cyclogenesis**
K A Browning, N M Roberts and A J Illingworth
June 1996

59. **Investigation of different representations of rain in a 1-d evaporation model**
H Swann
May 1996

60. **Parametrization of diabatic processes in the inversion of the omega-equation**
M Athanassiadou and A J Thorpe
June 1996

61. **The role of the environmental flow in the development of secondary frontal cyclones**
I A Renfrew, A J Thorpe and A Joly
June 1996

62. **Consequences of the geostrophic momentum approximation on barotropic instability**
S Malardel, A J Thorpe and A Joly
June 1996

63. **Contributions to the AMS/RMS Conference on Mesoscale Processes**
Reading, 9-13 September 1996

64. **Vorticity and potential vorticity in stratified flows interacting with an isolated obstacle**
Jorge A Gutiérrez and A J Thorpe
September 1996

65. **Triple point development: two case studies**
Douglas Parker
September 1996

66. **Radar observations of wind-shear splitting within evolving atmospheric Kelvin-Helmholtz billows**
D Chapman and K A Browning
April 1997

67. **Cold frontal structure derived from radar wind profilers**
K A Browning, D Jerrett, J Nash, T Oakley and N M Roberts
May 1997

68. **The dry intrusion and its effect on the frontal, cloud and precipitation structure of extratropical cyclones**
K A Browning - Text of invited special lecture at the Spring Conference
of the Meteorological Society of Japan, University of Tsukuba, 22 May 1997

69. **Met. Office Unified Model data, diagnostics, graphics programs, and other observational data available from the JCMM through the aegis of the Universities Weather Research Network (UWERN).** (Plus supplement)
Peter Panagi and Ed Dicks
June 1997

70. **Contributions of the JCMM/Dept of Meteorology Radar Group to the 28th AMS Radar Meteorology Conference.** Austin, Texas
September 1997

71. **Sensitivity of short-range weather forecasts to local potential vorticity modifications**
Meral Demirtas and Alan Thorpe
July 1997

72. **Objective identification of frontal wave cyclones**
T D Hewson
August 1997

73. **Attribution and its application to mesoscale structure associated with tropopause folds**
A J Thorpe
September 1997

74. **The role of the environmental flow in the development of secondary frontal cyclones**
Ian A Renfrew, Alan J Thorpe and Craig H Bishop
September 1997

75. **Potential vorticity: a short history of its definitions and uses**
Alan J Thorpe and Hans Volkert
September 1997

76. **Superposing semi-geostrophic potential vorticity anomalies**
H R Birkett and A J Thorpe
September 1997

77. **Short period forecasting of catchment-scale precipitation.**
Part 1: the role of Numerical Weather Prediction
M A Pedder, M Haile and A J Thorpe
September 1997

78. **Verification of the tracking technique used in an experimental cloud motion wind inferring system**
Z Wang, K A Browning and G A Kelly
October 1997

79. **A preliminary study of Fourier series analysis for cloud tracking with GOES high temporal resolution images**
Z Wang
October 1997

80. **Analysis of an ex-tropical cyclone after reintensifying as a warm-core extratropical cyclone**
K A Browning, G Vaughan and P Panagi
November 1997

81. **A JCMM overview of FASTEX IOPs**
S A Clough, H W Lean, N M Roberts, H Birkett, J-P Chaboureau, R Dixon, M Griffiths, T D Hewson and A Montani
January 1998

82. **Programs for PV inversion and modification**
Meral Demirtas
December 1997

83. **Release of potential shearing instability in warm frontal zones**
D Chapman and K A Browning
February 1998

84. **The European Cloud-Resolving Modelling Programme (EUCREM)**
Summary Report from the coordinator
P W White
April 1998

85. **A frontal wave database**
T D Hewson
April 1998

86. **Layering observed in dropsoundings from IOP 1 of Fronts 92**
S A Clough
May 1998

87. **Use of wind-shear displays for Doppler radar data**
D Chapman and K A Browning
May 1998

88. **Radar estimates of rainfall rates at the ground in bright band and non-bright band events**
T J Smyth and A J Illingworth
June 1998

89. **Correction for attenuation of radar reflectivity using polarisation data**
T J Smyth and A J Illingworth
June 1998

90. **The effects of convection on chemical reactions and precipitation scavenging**
Neil R Gimson
July 1998

91. **How to use the display program DISP**
Nigel Roberts
August 1998

92. **Conceptual models of cyclogenesis**
Adrian T Semple
August 1998

93. **Observations of oblate hail using dual polarisation radar and implications for hail detection schemes**
T J Smyth, T M Blackman and A J Illingworth
September 1998

94. **The semigeostrophic diagnosis of vertical motion. Part I: Formulation and co-ordinate transformations**
Mike A Pedder and Alan J Thorpe
September 1998

95. **The semigeostrophic diagnosis of vertical motion. Part II: Results for an idealised baroclinic wave life cycle**
Alan J Thorpe and Mike A Pedder
September 1998

96. **Convective destabilisation by a tropopause fold diagnosed using potential vorticity inversion**
Morwenna Griffiths, Alan Thorpe and Keith Browning
October 1998

97. **Forecast skill of the ECMWF model using targeted observations during FASTEX**
A Montani, A J Thorpe, R Buizza and P Unden
October 1998

98. **Observations and model simulations of the FASTEX IOP 16 frontal wave - effects of sublimation**
Sid A Clough, Humphrey W Lean, Nigel M Roberts and Richard M Forbes
December 1998

99. **The application of conceptual models in NWP**
Adrian T Semple
January 1999

100. **Mesoscale analysis of arc rainbands in a dry slot**
K A Browning and N M Roberts
January 1999

101. **Interaction of mesoscale tropopause depressions with a warm-core cyclone: observational and model analyses, and sensitivity to analysis errors**
K A Browning, A J Thorpe, A Montani, D Parsons, M Griffiths, P Panagi and E M Dicks
February 1999

102. **The use of water vapour imagery and PV inversion to adjust initial conditions in NWP**
Sean J Swarbrick
February 1999
This report is no longer available; see Internal Report No.108

103. **Summary notes for a lecture course on Waves in the Atmosphere and Ocean**
A A White
March 1999

104. **Results of a questionnaire on the operational value of conceptual models (CMs) of fronts and cyclones**
N M Roberts & M V Young
July 1999

105. **Contributions to the Poster Session at the 1998 UWERN Annual Science Meeting**
assembled by A A White
August 1999

106. **The objective analysis of dropsonde data from FASTEX**
Richard Forbes, Sid Clough, Mark Dixon, Andy Macallan & Nigel Roberts
January 2000

107. *NWP Technical Report No.302*
Implications for Mesoscale Modelling from a Study of the FASTEX IOP 16 Mid-latitude Cyclone
Richard M Forbes, Humphrey W Lean, Nigel M Roberts and Peter A Clark
March 2000

108. *NWP Technical Report No.291*
The use of water vapour imagery and PV inversion to adjust initial conditions in NWP
Final Project Report
Sean J Swarbrick
September 1999

109. *NWP Technical Report No.294*
A guide to aspects of water vapour imagery interpretation: the significance of dry regions
Nigel M Roberts
January 2000

110. *NWP Technical Report No.300*
The relationship between water vapour imagery and thunderstorms
Nigel M Roberts
February 2000

111. *NWP Technical Report No.293*
Holomorphic structures in hydrodynamical models of nearly geostrophic flow
V N Roubtsov and I Roulstone
January 2000

112. *NWP Technical Report No.301*
Multi-sensor synthesis of the mesoscale structure of a cold-air comma cloud system
K A Browning, P Panagi and E M Dicks
March 2000

113. *NWP Technical Report No.307*
Observations of stratospheric air entering the circulation of a polar low
K A Browning and E M Dicks
May 2000

114. *NWP Technical Report No.309*
Wind profiler – Unified Model comparison statistics
Peter Panagi & Ed Dicks
March 2000

115. *NWP Technical Report No.310*
Towards a similarity theory of moist convective updrafts
Olaf Stiller and George C Craig
May 2000

116. *NWP Technical Report No.312*
The mystery of striated cloud heads in satellite imagery
R S Dixon, K A Browning and G J Shutts
April 2000

117. *NWP Technical Report No.313*
MDIAG: a Fortran 90 program to compute diagnostics on pressure levels from Unified Model data on model levels
Peter Panagi
June 2000

118. *NWP Scientific Paper No.56*
Rearrangements of functions with applications to meteorology and ideal fluid flow
R J Douglas
June 2000

119. *NWP Technical Report No.320*
Tests of New Dynamics Model on the FASTEX IOP16 case
Humphrey Lean
September 2000

120. *NWP Scientific Paper 57*
A classification of FASTEX cyclones using a height-attributable QG vertical motion diagnostic
A C L Deveson, K A Browning, T D Hewson
September 2000

121. *NWP Scientific Paper 59*
Measurements of dissipation rate in frontal zones
D.Chapman, K A Browning
August 2000

122. *NWP Technical Report 331*
Not Issued yet

123. *NWP Technical Report 337*
A Case Study of High Resolution Fog Forecasts with the New Dynamics
P. Clark
November 2000

124. *NWP Technical Report 338*
Comparison of ECMWF Winter-Season Cloud Fraction with Radar Derived Values
Robin J. Hogan, Christian Jakob, Anthony J. Illingworth
January 2001

125. *NWP Technical Report 339*
Deriving Cloud overlap statistics from radar
Robin J. Hogan, Anthony J. Illingworth
January 2001

126. *NWP Technical Report 344*
Results from simulations of an organised convective event using the New Dynamics at 12, 4 and 2km resolution.
Nigel Roberts
January 2001

127 *NWP Technical Report 348*
A North Atlantic Survey of Cyclogenesis in 1999: Unified Model Performance in Short Range Forecasts & The Relationship Between Potential Vorticity, Water Vapour Imagery and Analysis Accuracy.
Adrian Semple
March 2001

128 NWP Scientific Paper 61
Are there higher-accuracy analogues of semigeostrophic theory?
Ian Roulstone, Michael E. McIntyre
June 2001

129 NWP Scientific Paper 62
Stacked slantwise convective circulations
K A Browning, D Chapman, R S Dixon
April 2001

Met Office Joint Centre for Mesoscale Meteorology Department of Meteorology
University of Reading PO Box 243 Reading RG6 6BB United Kingdom
Tel: +44 (0)118 931 8425 Fax: +44 (0)118 931 8791
www.metoffice.com